Synapses and Ca^{2+} activity in oligodendrocyte precursor cells can predict where myelin sheaths form

Jiaxing Li[1, *], Tania Miramontes[1], Tim Czopka[2], Kelly R. Monk[1, *]

1 Vollum Institute, Oregon Health & Science University, Portland, OR, USA

2 Centre for Clinical Brain Sciences, University of Edinburgh, Edinburgh, UK

*Corresponding authors

SUMMARY

In the nervous system, only one type of neuron-glial synapse is known to exist: that between neurons and oligodendrocyte precursor cells (OPCs). Neuron-OPC synapses are thought to bridge neuronal activity to OPCs. However, their composition, assembly, downstream signaling, and *in vivo* functions remain largely unclear. Here, we use zebrafish to address these questions and identify postsynaptic molecules PSD-95 and Gephyrin in OPCs. They increase during early development and decrease upon OPC differentiation. PSD-95 and Gephyrin in OPCs are highly dynamic and frequently assemble at "hotspots." Gephyrin hotspots and synapse-associated Ca^{2+} activity in OPCs predict where a subset of myelin sheaths form in oligodendrocytes. Further analyses reveal that spontaneous synaptic release is integral to OPC Ca^{2+} activity, while evoked synaptic release contributes only in early development. Finally, disruption of the synaptic genes *dlg4a&b*, *gephyrinb*, and *nlgn3b* impairs OPC differentiation and myelination. Together, we propose that neuron-OPC synapses are dynamically assembled and can predetermine myelination patterns through Ca^{2+} signaling.

45 **INTRODUCTION**

46 Oligodendrocyte precursor cells (OPCs) are a dynamic cell type in the central nervous system
47 (CNS) that can migrate, proliferate, dramatically remodel processes, and differentiate into
48 myelinating oligodendrocytes. OPCs and their interactions with neurons play important roles in
49 CNS health and disease such as myelination and remyelination[1], neural network remodeling[2],
50 and glioma progression[3]. Synapses form between neurons (presynaptic) and OPCs (postsynaptic)
51 and represent the only type of glial synapse in the nervous system. The composition of neuron-
52 OPC synapses is largely unknown, with the exception of some synaptic receptors (*e.g.*,
53 glutamatergic and GABAergic) that were revealed by pharmacology and electrophysiology[4].
54 Neuron-OPC synapse assembly and regulation *in vivo* are mysterious, due in part to a paucity of
55 tools to label these structures. Previous studies knocking down single synaptic receptor types
56 found diverse and sometimes conflicting effects on OPC development and myelination; for
57 example, blocking NMDA receptors reduced or had no effect on myelination[5,6], and blocking
58 GABA receptors enhanced or had no effect on OPC proliferation[7,8]. This is possibly due to
59 redundancy, as OPCs possess multiple synaptic receptors[4]. Currently our understanding of the
60 functions of neuron-OPC synapses is incomplete.

61 OPCs are hypothesized to sense the activity of neurons through neuron-OPC synapses.
62 Several studies support this idea: neuronal activity can modulate OPC development and
63 myelination[9–13]; axonal stimulation in *ex vivo* rodent studies was reported to cause synapse-
64 dependent Ca^{2+} increases in oligodendrocyte lineage cells, mostly in somas[14–16]. However, the
65 *in vivo* relationship between neuronal activity, neuron-OPC synapses, and OPC Ca^{2+} activity

66 without exogenous stimulation is unknown. Furthermore, the role of synapses in forming
67 microdomain (MD) Ca^{2+} events in OPC processes[17,18] has not been addressed.
68 Here we identify postsynaptic scaffold proteins membrane-associated guanylate
69 kinases (MAGUKs) and Gephyrin in zebrafish OPCs. The postsynaptic puncta number in OPCs
70 increases during early development, reduces upon OPC differentiation, and exhibits small
71 differences across CNS regions but no differences between OPC subgroups. *In vivo* imaging of
72 PSD-95-GFP (a MAGUK member) and GFP-Gephyrin puncta in OPCs reveals that the puncta are
73 highly dynamic, presumably resulting in extensive synaptic coverage. Although dynamic,
74 postsynaptic puncta repeatedly assemble at approximately 10 hotspots per OPC. GFP-Gephyrin
75 hotspots at the OPC stage predict where a subset of myelin sheaths form at the
76 oligodendrocyte stage, in a synaptic release-dependent manner. Further analysis reveals that
77 Ca^{2+} activity is associated with neuron-OPC synapses and similarly predicts where myelin
78 sheaths form. The majority of *in vivo* OPC Ca^{2+} events occur in MDs, require spontaneous
79 synaptic release, and, during early development, require evoked synaptic release from neurons.
80 Finally, we find that disruption of synaptic genes, *dlg4a&b*, *gephyrinb*, and *neuroligin3b* (*nlgn3b*)
81 impairs OPC development and myelination. Collectively, these results suggest that neuron-OPC
82 synapses partially predetermine myelination patterns through preferential assembly and Ca^{2+}
83 signaling.
84

85 ## RESULTS

86 **Postsynaptic organizers MAGUK/PSD-95 and Gephyrin are present in zebrafish spinal cord**
87 **OPCs**

88 Transcript expression of *Dlg4* (encodes PSD-95, often associated with excitatory
89 Glutamate receptors) and *Gephyrin* (often associated with inhibitory GABA and Glycine
90 receptors) were previously reported in zebrafish and mammalian OPCs (Extended Data Fig. 1a-
91 b)[17,19]. We detected the presence of MAGUK/PSD-95 and Gephyrin puncta in zebrafish spinal
92 cord OPCs using immunohistochemistry (IHC) at 3 days post-fertilization (dpf) (Fig. 1a-c and
93 Extended Data Fig. 1c) and found that puncta were localized to OPC processes and somas
94 (Extended Data Fig. 1d). Next, we visualized postsynaptic puncta using Fibronectin intrabodies
95 generated by mRNA display (FingRs) that bind to endogenous PSD-95 and Gephyrin *in vivo*[20].
96 We found FingR.GFP enrichment in somas (Fig. 1d), similar to previous reports in neurons[20–22].
97 More importantly, we observed puncta labeling in OPC processes (Fig. 1d), indicating potential
98 synaptic locations. By IHC and FingRs, we identified 18.2 ± 2.5 and 20.3 ± 2.4 MAGUK/PSD-95
99 puncta, respectively, and 29.2 ± 3.1 and 21.1 ± 4.0 Gephyrin puncta, respectively, per OPC at 3
100 dpf (Fig. 1e). The similar results from two distinct methods support the presence of
101 postsynaptic puncta in OPCs and extend previous work that reported PSD-95 in myelin
102 sheaths[23].
103 Given that OPCs are heterogeneous according to transcriptomic and electrophysiological
104 studies[24,25], we examined the number of postsynaptic puncta across developmental stages and
105 CNS regions using IHC. We observed an increasing trend through development: both MAGUK
106 and Gephyrin puncta numbers increased from 2 dpf (10.4 ± 1.8 MAGUK; 15.9 ± 2.1 Gephyrin) to
107 5 dpf (28.8 ± 8.6 MAGUK; 68.2 ± 6.7 Gephyrin) (Extended Data Fig. 2a). The postsynaptic puncta
108 numbers per cell were overall similar across CNS regions, except that Gephyrin puncta numbers
109 were higher in the forebrain and midbrain (20.2 ± 1.2) compared to the spinal cord (13.8 ± 0.9)

110 (Extended Data Fig. 2b), possibly suggesting a preference of OPCs to form synapses with
111 inhibitory neurons in the brain. Within the zebrafish spinal cord, OPC subgroups were
112 previously reported to reside in neuron-rich vs. axon and synapse-rich regions (Extended Data
113 Fig. 2c)[17]. We found that postsynaptic puncta numbers were similar between these OPC
114 subgroups (Extended Data Fig. 2d).

115 **Some but not all MAGUK and Gephyrin puncta in OPCs are associated with other synaptic**
116 **molecules**

117 Next, we tested whether these puncta align with presynaptic structures. Using the pan-
118 presynaptic marker Synapsin (Fig. 2a-f), we identified MAGUK and Gephyrin puncta in OPCs that
119 aligned (Fig. 2b, e) or that did not align (Fig. 2c, f) with Synapsin. 46.1 ± 7.4% and 38.3 ± 4.8% of
120 MAGUK and Gephyrin puncta in an OPC, respectively, aligned with Synapsin in the spinal cord,
121 and a similar percentage of puncta in an OPC aligned with Synapsin in other CNS regions (Fig.
122 2g). In addition, at 3 dpf, 42.1 ± 4.8% of Gephyrin puncta in an OPC aligned with Glycine
123 receptors (Fig. 2h-i). We noted that postsynaptic markers in individual OPCs exhibited a wide
124 range of alignment with presynaptic molecules (0-100%). Altogether, the alignment of MAGUK
125 and Gephyrin puncta with other synaptic molecules varies from OPC to OPC, and averages 40-
126 60% throughout the CNS.

127 ***In vivo* imaging reveals downregulation of PSD-95-GFP and GFP-Gephyrin upon OPC**
128 **differentiation**

129 To understand synapse assembly and disassembly in OPCs, we conducted *in vivo* time-
130 lapse imaging. We found that FingR.GFP tools were especially susceptible to photobleaching
131 during long-term imaging; we therefore generated PSD-95-GFP and GFP-Gephyrin constructs

132 and drove their expression with *sox10*, a pan-oligodendrocyte lineage promoter that also labels
133 a subset of interneurons. At 3 dpf in the spinal cord, we found both markers present in
134 punctate and cytosolic forms in OPCs (Fig. 3a), consistent with patterns observed in neurons[26,27].
135 PSD-95-GFP and GFP-Gephyrin puncta size in OPCs resembled that of neurons (Fig. 3a-b and
136 Extended Data Fig. 3a). GFP was enriched in somas, a known phenomenon observed with GFP-
137 tagging and knock-in synaptic labeling[28–35]. It is difficult to resolve puncta with such enrichment;
138 therefore, we excluded somas from our analyses. We conducted a series of analyses including
139 puncta number quantification, correlation between puncta number and GFP-tagged protein
140 levels, synaptic alignment, developmental changes, and GFP colocalization with antibody
141 staining (Fig. 1e, 2g and Extended Data Fig. 2a, 3b-i). By every applicable metric, we found that
142 PSD-95-GFP and GFP-Gephyrin are similar to endogenous labeling by IHC and FingR.GFP. Next,
143 we examined if these puncta were regulated upon OPC differentiation. We tracked individual
144 OPCs over the course of their development and quantified the GFP-tagged puncta number.
145 Because OPC differentiation takes several hours for all processes to either retract or transform
146 into nascent myelin sheaths[36,37], we used the disappearance of the last exploratory process as a
147 reference point. We found a decreasing trend during OPC differentiation: puncta numbers
148 reduced from 9.8 ± 2.5 PSD-95-GFP and 16.5 ± 2.8 GFP-Gephyrin to 3.9 ± 1.2 PSD-95-GFP and
149 9.1 ± 2.0 GFP-Gephyrin (Fig. 3c-d). In cases where we observed differentiating oligodendrocytes
150 that possessed both processes and myelin sheaths, PSD-95-GFP and GFP-Gephyrin puncta were
151 4-fold and 3.3-fold more enriched in processes than in sheaths, respectively (Fig. 3e-f),
152 suggesting preferential localization of synaptic puncta to processes rather than nascent myelin
153 sheaths. Altogether, these results show a downregulation of GFP-tagged postsynaptic puncta

154 upon OPC differentiation, consistent with reduced synaptic inputs reported from *ex vivo*
155 electrophysiological studies in rodents[38,39].

156 **PSD-95-GFP and GFP-Gephyrin puncta in OPCs are dynamic and repeatedly assemble at**
157 **hotspots**

158 We next sought to analyze the dynamics of PSD-95-GFP and GFP-Gephyrin in OPCs *in*
159 *vivo*. These GFP-tagged puncta in OPCs were dynamically assembled and disassembled during
160 an 11-hour imaging session, while those in neurons remained relatively stable (Fig. 4a and
161 Supplementary Video 1). The number of puncta per cell remained similar in neurons, but
162 fluctuated in OPCs over 30 minutes of observation (Fig. 4b). Individual GFP-tagged puncta in
163 neurons lasted about 234 min (PSD-95-GFP) and 206 min (GFP-Gephyrin), while those in OPCs
164 lasted about 12 min (PSD-95-GFP) and 5 min (GFP-Gephyrin) (Fig. 4c). Although photobleaching
165 occurs in FingR.GFP-expressing cells over long periods, short-term imaging is possible. We were
166 therefore able to examine puncta dynamics with FingR.GFP, and found similar puncta duration
167 compared to GFP-tagging (Fig. 4c). Next, we examined the spatial distribution of GFP-tagged
168 puncta by tracking them in individual OPCs (Fig. 4d). Over the course of 7 hours, GFP-Gephyrin
169 puncta covered a large space, with a convex hull volume nearly 50 times the volume of an OPC
170 from a single timepoint (Fig. 4d-e). Yet this convex hull volume was not significantly different
171 from the convex hull volume of the OPC over the imaging window, suggesting that GFP-
172 Gephyrin assembly stays tuned with OPC process remodeling (Fig. 4d-e). Puncta assembly and
173 disassembly occurred in process regions that were relatively stable as well as those that were
174 remodeled over the imaging window (Fig. 4f-g), suggesting that GFP-tagged puncta dynamics in
175 OPCs were not simply caused by process remodeling. Altogether, GFP-tagged postsynaptic

176 puncta assemble dynamically and cover a large space over time in tune with OPC process
177 remodeling.

178 Multiple appearances of puncta in the same area (Fig. 4f-g) raises the question if specific
179 regions are preferred for synaptic assembly. To test this, we plotted PSD-95-GFP and GFP-
180 Gephyrin puncta over time and overlaid heatmaps of puncta frequencies (Fig. 4h-i). We found
181 approximately 10 regions (1 µm x 1 µm x 4 µm volumes) per OPC where multiple puncta
182 appeared frequently (3 standard deviations above the average), and refer to these regions as
183 hotspots (Fig. 4j). Hotspots represented only 0.3% of GFP-Gephyrin puncta space coverage (Fig.
184 4e). These results suggest that some postsynaptic puncta in OPCs assemble repeatedly and
185 preferentially in the confined spaces of hotspots.

186 **GFP-Gephyrin hotspots in OPCs predict a subset of future myelin sheath formation in a**
187 **synaptic release-mediated manner**

188 In the zebrafish spinal cord, a myelinating oligodendrocyte forms an average of 10
189 myelin sheaths[36], similar to the hotspot number we observed per OPC. We wondered if these
190 hotspots in OPCs were associated with future myelin sheath formation. To test this, we
191 conducted long-term imaging of individual OPCs that differentiated and myelinated axons
192 (Supplementary Video 2) and measured the distances from GFP-Gephyrin hotspot centers
193 (centroids of 1 µm x 1 µm x 4 µm) to future myelin sheaths (Fig. 5a-d, see Methods). In
194 comparison, we selected 30 representative points outside hotspots (nonhotspot) in an OPC
195 (See Methods). The hotspots were mostly in proximity to future myelin sheaths (Fig. 5e), and
196 the hotspot-sheath distance was significantly smaller than the nonhotspot-sheath distance (Fig.
197 5f). Further, we examined the percentage of hotspots or nonhotspots that predicted where

198 future myelin sheaths formed. We chose 1 µm as a threshold because we analyzed previous EM
199 datasets[40] and our IHC images and found a distance of 1.4-1.6 µm between two myelinated
200 axons in the dorsal spinal cord (Extended Data Fig. 4a-c). Within 1 µm, 29.6 ± 8.7% of hotspots
201 in an OPC predicted future sheath locations, while only 5.9 ± 3.4% of nonhotspots did (Fig. 5g).
202 Consistent with this result, 31.2 ± 7.1% of puncta in the hotspot region predicted future myelin
203 sheaths, significantly higher than the prediction by puncta outside (15.1 ± 3.4%) or by chance
204 (5.5 ± 1.1%, myelin volume / OPC survey volume) (Extended Data Fig. 4d-e). In addition, 14.1 ±
205 2.7% of future myelin sheaths in oligodendrocytes were predicted by hotspots in OPCs
206 (Extended Data Fig. 4f), suggesting that hotspots in OPCs predict a subset of myelin sheath
207 formation.

208 Next, we asked if the relationship between OPC hotspots and future myelin sheaths was
209 dependent on synaptic release. We blocked synaptic release by injecting tetanus toxin (TeNT)
210 into ventricles between 2-3 dpf (Fig. 5c). We verified the TeNT delivery to OPCs in the CNS with
211 Dextran injection (Extended Data Fig. 4g; see Methods). TeNT administration caused a right-
212 shift in hotspot-sheath distance distribution (Fig. 5e). The hotspot-sheath distance was no
213 longer significantly smaller than the nonhotspot-sheath distance (Fig. 5f). More importantly,
214 TeNT administration reduced the hotspots' prediction of myelin sheaths (Fig. 5g), the prediction
215 of myelin sheath by GFP-Gephyrin puncta in the hotspot regions (Extended Data Fig. 4e), and
216 the percentage of myelin sheaths predicted by hotspots (Extended Data Fig. 4f). This was not
217 due to changes in OPC convex hull volume, OPC hotspot number, or myelin sheath number
218 (Extended Data Fig. 4h-j). Together, these results suggest that GFP-Gephyrin hotspots can
219 predict myelin sheath locations in a synapse-release dependent manner.

220 Recent work suggests that early myelination exhibits dynamic and transient
221 ensheathments[41]. We similarly observed this phenomenon (Extended Data Fig. 4k) and
222 wondered if the OPC hotspots could predict transient ensheathments. We found that within 1
223 µm, 32.5 ± 7.1% of hotspots in an OPC predicted future transient ensheathment locations in a
224 synapse-release dependent manner (Extended Data Fig. 4l-n). More importantly, when we
225 combined all ensheathments (stable sheaths and transient ensheathments), 44.2 ± 9.7% of
226 hotspots in an OPC predicted future sheath locations in a synapse-release dependent manner
227 (Fig. 5h-j). This percentage is higher than prediction by either stable sheaths or transient
228 ensheathments, but lower than the combination of two, suggesting that some hotspots can
229 predict both stable sheaths and transient ensheathments, while others predict only one type.

230 **OPC Ca^{2+} activity is associated with synapses and predicts myelin sheath formation**

231 Given the role of Ca^{2+} signaling in sheath remodeling[18,42], we examined the relationship
232 of Ca^{2+} signaling events with synapses and sheath formation *in vivo*. With a plasma membrane-
233 targeted GCaMP6s, we analyzed OPC Ca^{2+} activity at single-cell resolution *in vivo* (Fig. 6a-b). We
234 found that 99% of Ca^{2+} events in OPCs occurred in MDs on processes, and 97% of OPCs
235 exhibited only MD Ca^{2+} activity during our recordings (Fig. 6c, Supplemental Video 3-4),
236 consistent with recent work in mammals[43,44]. We examined the proximity between Ca^{2+} events
237 in MDs and a presynaptic marker, synaptophysin-RFP[17]. Through 3D reconstruction, we found
238 that 42 ± 6% of MD Ca^{2+} events were within 0.5 µm proximity to synaptophysin-RFP puncta at 5
239 dpf (Fig. 6d-e). We also observed that some Ca^{2+} events initiated from a "puncta"-like region in
240 proximity to synapses (Fig. 6f-g). Next, we performed time-lapse imaging to measure the
241 distance from MD Ca^{2+} events in an OPC to sheaths formed after the OPC differentiated and

242 myelinated axons (Fig. 6h-i). In comparison, we selected 30 representative points outside MDs
243 (nonMD) in an OPC (See Methods). The MD-sheath distance was significantly smaller than the
244 nonMD-sheath distance (Fig. 6j). Next, we examined the percentage of MDs that predicted
245 where myelin sheaths formed. Within 1 µm, 32.0 ± 9.4% of MDs in an OPC predicted future
246 sheath locations, while only 4.3 ± 1.2% of nonMDs did (Fig. 6k). These measurements of MD-
247 future sheath are similar to those of hotspots-future sheath, suggesting that MD Ca^{2+} activity in
248 OPCs *in vivo*, along with Gephyrin hotspots, predetermines where a subset of myelin sheaths
249 form.

250 **Synaptic release contributes to generating OPC Ca^{2+} activity *in vivo***

251 Given the close relationship between Ca^{2+} activity and synapses, we investigated the
252 role of synapses in OPC Ca^{2+} activity *in vivo.* We blocked synaptic release by sparsely expressing
253 tetanus toxin light chain (TeNTlc)-tdtomato[45] in axons at 5 dpf (Fig. 7a). Compared to OPCs that
254 neighbored few TeNTlc-expressing axons (< 4, few), those that neighbored many TeNTlc-
255 expressing axons (> 4, many) exhibited significantly reduced frequency of Ca^{2+} activity (0.013 ±
256 0.002 vs. 0.020 ± 0.002 Hz), peak amplitude (1.4 ± 0.08 vs. 1.81 ± 0.12 fold), basal signal
257 intensity (0.74 ± 0.06 vs. 1.00 ± 0.10), and MD length (6.00 ± 0.25 vs. 7.03 ± 0.38 µm) (Fig. 7b-c
258 and Extended Data Fig. 5a). Next, we delivered tetanus toxin (TeNT) proteins to the CNS
259 through ventricle injection at 5 dpf and analyzed Ca^{2+} activity before and after injection (Fig. 7d).
260 We coinjected Dextran (MW 3,000) and verified that Dextran surrounded OPCs before Ca^{2+}
261 imaging (Fig. 7e). While control solution administration had no effect, TeNT administration led
262 to nearly 45% reduction in MD event number and frequency of Ca^{2+} activity (Fig. 7f, g, Extended
263 Data Fig. 5b and Supplementary Video 5). These results suggest an important role for synaptic

264 release in OPC Ca^{2+} activity. TeNT administration also increased peak duration and MD area,
265 suggesting that the synapse-dependent Ca^{2+} activity is associated with shorter duration and
266 smaller MDs.

267 These effects could be due to reduced neuronal activity and evoked synaptic release by
268 TeNT. But to our surprise, we found that blocking neuronal action potentials with the voltage-
269 gated Na^{+} channel blocker tetrodotoxin (TTX) had no effect on the OPC Ca^{2+} activity at 5 dpf (Fig.
270 7h and Extended Data Fig. 5c). We excluded the possibility of ineffective TTX delivery in three
271 ways: we observed larval paralysis within 3 minutes post-injection (30/30), a complete block of
272 motor neuron Ca^{2+} activity (Extended Data Fig. 5e-f), and dextran co-injected with TTX (dextran
273 MW3000, larger than TTX) surrounded the imaged OPCs (120/120). Therefore, the reduced Ca^{2+}
274 activity upon TeNT injection was most likely due to the effects of TeNT on spontaneous release
275 at neuron-OPC synapses, rather than neuronal activity. We did, however, observe reduced OPC
276 Ca^{2+} activity upon TTX injection at the earlier timepoint of 3 dpf (Fig. 7i and Extended Data Fig.
277 5d), consistent with a previous report[18] and suggesting a diminishing role of neuronal activity
278 and evoked synaptic release over development. Altogether, our results establish a role for
279 synaptic release in generating OPC Ca^{2+} activity *in vivo*.

280 **Disruption of postsynaptic molecules impairs OPC development and myelination.**

281 Previous studies found that blocking neuronal activity and presynaptic release could
282 impair myelination[10,12]. Given how GFP-Gephyrin assembly and Ca^{2+} activity in OPCs predict
283 myelin sheath formation in a synaptic release-dependent manner, we next sought to examine
284 the role of postsynaptic molecules in OPC development and myelination. We reasoned that
285 disruption of these molecules could impair OPCs development and myelination because

286 without them, OPCs would have to bypass the lack of presynaptic inputs to differentiate and
287 choose axons for myelination. We developed and verified a cell-specific CRISPR/Cas9-mediated
288 gene disruption system (Extended Data Fig. 6). Besides *dlg4a&b* and *gephyrinb* (See Methods),
289 which are important for excitatory and inhibitory synapses, respectively, we also targeted
290 *neuroligin3* (*nlgn3*), because it is highly expressed in OPCs (Extended Data Fig. 1a-b)[17,19],
291 localized to neuron-OPC synapses (Extended Data Fig. 7a-d), important for MAGUK and
292 Gephyrin density (Extended Data Fig. 7e-f), and Ca^{2+} activity in OPCs (Extended Data Fig. 7g-i).
293 To examine if OPC differentiation is affected by disruption of these postsynaptic molecules, we
294 calculated the ratio of myelinating oligodendrocytes at different stages of development and
295 found that *nlgn3b* disruption in oligodendrocyte lineage cells led to fewer myelinating
296 oligodendrocytes and more OPCs (Fig. 8a-c). To assess myelination, we measured the number
297 and total length of nascent myelin sheaths. *dlg4a&b*- or *gephyrinb*-disruption reduced the total
298 length of myelin sheaths at 5 dpf (Fig. 8d-f). *nlgn3b*-disruption resulted in a reduction of the
299 number and total length of myelin sheaths at both 3 dpf and 5 dpf (Fig. 8d-f and Extended Data
300 Fig. 8a-b). Overexpression of a presumed dominant-negative Nlgn3b (Δ116) that lacks c-
301 terminal domains required for interaction with MAGUK and Gephyrin[23,46] (Extended Data Fig. 8c)
302 also led to a reduction of the total length of myelin sheaths (Fig. 8f). In addition, among
303 myelinating oligodendrocytes, we noted that 7.6 ± 1.8% upon *nlgn3b* disruption possessed
304 cytoplasmic processes with abnormal trapezoidal structures (Fig. 8g and Extended Data Fig. 8d-
305 e), suggestive of defective OPC differentiation. Together, these results support a role for
306 postsynaptic molecules in proper OPC differentiation and myelination.
307

308 **DISCUSSION**

309 The landmark discovery of neuron-OPC synapses over 20 years ago has inspired a
310 number of studies to examine their properties with electrophysiology and EM[4], yet we still lack
311 basic understanding of their assembly and function. Here, we establish an *in vivo* model of
312 these synapses in zebrafish OPCs (Fig. 8h): they are composed of postsynaptic MAGUK (PSD-95)
313 and Gephyrin and are developmentally regulated; they exhibit a wide range of alignment with
314 synaptic partners and dynamic synapse features; they cover large spatial volumes over time but
315 frequently and repeatedly assemble at specific and confined "hotspots;" Gephyrin hotspots and
316 synaptic release-mediated Ca^{2+} activity partially predict myelination patterns; and disruption of
317 the synaptic molecules PSD-95, Gephyrin, and Nlgn3 impairs OPC development and myelination.

318 Previous studies suggest that neuronal activity and presynaptic release bias
319 oligodendrocyte myelination to "active" axons[10,12]. However, it is not clear what mechanisms
320 mediate this preference. Here, we identify a postsynaptic mechanism in OPCs that depends on
321 presynaptic release and predicts future myelination, which might partially explain how
322 neuronal activity regulates myelination. We observed an approximately 30% predication rate
323 with 1 µm threshold by both GFP-Gephyrin hotspots and MD Ca^{2+} in OPCs, suggesting they may
324 act in the same pathway to determine where myelin sheaths form. One possible scenario is that
325 presynaptic release from neurons leads to synaptic activation in a nearby OPC process and
326 subsequent Ca^{2+} activity in MDs. After the OPC "senses" this neuronal location, it could enhance
327 the synaptic assembly in this location through Ca^{2+} signaling. Through such a positive-feedback
328 mechanism, "hotspots" form, while the pre- and post-synaptic interactions influence the
329 cytoskeleton to transform a process into a myelin sheath. 14% of stable myelin sheaths were

330 predicted by GFP-Gephyrin hotspots, suggesting specificity in prediction and other factors or
331 mechanisms involved, such as PSD-95 hotspots, neurotransmitters, or cell adhesion molecules.
332 During OPC differentiation, we and others observed transient ensheathments that disappear
333 rapidly after formation[47]. The GFP-Gephyrin hotspots predict the formation of transient
334 ensheathments as well as the stable sheaths, suggesting that similar postsynaptic mechanisms
335 in OPCs guide both transient ensheathment and stable myelin sheath formation. What type of
336 presynaptic release is involved in predetermining myelination patterns? Multiple
337 neurotransmitters and neuropeptides can regulate the development of oligodendrocyte lineage
338 cells[5–8,48]. Therefore, different types of neurons across CNS regions may employ a combination
339 of neurotransmitters and/or neuropeptides to influence myelination of their axons. Here, we
340 focus on Gephyrin-containing synapses and predict that inhibitory neurotransmitters, such as
341 glycine and GABA, may be involved in regulating the dynamic assembly of Gephyrin and OPC
342 development. Meanwhile, how the presynaptic release sites apposed to OPC postsynaptic sites
343 are distributed in neurons is still not fully understood. A recent study suggests presynaptic
344 release sites are assembled in hotspots towards which myelin sheaths grow[49]. Together with
345 our data, this suggests that both pre- and post-synaptic sites of neuron-OPC synapses are
346 dynamically assembled at "hotspots" that predetermine where future myelin sheaths form on
347 axons. The pre- and post-synaptic alignment at OPC synapses averages 40-50%, suggesting that
348 some synaptic locations miss other synaptic molecules and are likely immature[50–53]. Such
349 alignment ratios and fast synaptic assembly are in tune with an OPC's dynamic cell biological
350 properties and could allow these cells to effectively survey their environments.

351 Several studies have identified synaptic mechanisms underlying Ca^{2+} elevation in OPCs
352 under conditions of increased neuronal activity (*e.g.*, through axon stimulation) with a focus on
353 somal activity[14–16,54]. Interestingly, recent studies provided evidence that neuronal activity or
354 synaptic release contribute little to OPC MD Ca^{2+} activity in adult mice brains[43,44]. Like these
355 studies, we find that OPC Ca^{2+} activity *in vivo* mainly occurs in MDs; in contrast, we show that
356 MD Ca^{2+} activity does require synaptic release in the zebrafish spinal cord, suggesting
357 interesting regional and/or developmental differences that will be important for future study.
358 Neuronal activity and evoked synaptic release play a role in OPC Ca^{2+} activity at 3 dpf, but to our
359 surprise not at 5 dpf. Considering that OPC differentiation initiates at 3 dpf, this suggests that
360 OPCs are sensitive to neuronal activity through Ca^{2+} signaling at this critical stage of
361 development. This sensitivity may be important for OPC differentiation and myelination in
362 development. This development-specific sensitivity to neuronal activity also cautions the usage
363 of axon stimulation that has been widely used in previous studies of OPC Ca^{2+} activity[14–16,54]. In
364 our Ca^{2+} assays, we observe "outlier" OPCs that behave differently from the majority of OPCs.
365 For example, some OPCs exhibit no change or even an increase of Ca^{2+} activity upon TeNT
366 treatment or TTX treatment while most OPCs exhibit reduction. These "outlier" OPCs and
367 activity could be due to Ca^{2+} generated from synapse-independent mechanisms, such as
368 adrenergic receptor-mediated Ca^{2+} activity as recently suggested in cerebral cortex[43,44]. In line
369 with this, nearly 61% of Ca^{2+} MDs do not associate with presynaptic markers, and nearly 55%
370 residual Ca^{2+} activity remains after TeNT treatment, supporting synapse-independent Ca^{2+}-
371 inducing mechanisms in OPCs as well as synapse-dependent mechanisms.

372 Our findings that *dlg4a&b*, *gephyrinb*, or *nlgn3b* knockdown in oligodendrocyte lineage
373 cells impairs OPC differentiation and myelination suggests a potential role of synapses in OPCs.
374 This is consistent with our observations that GFP-Gephyrin hotspots and Ca^{2+} MDs in OPCs
375 predict where myelin sheaths form in oligodendrocytes. The myelination defects were not
376 detected until 5 dpf with *dlg4a&b* or *gephyrinb* knockdown, but were detected at both 3 and 5
377 dpf with *nlgn3b* knockdown. We reasoned that this was due to Nlgn3's broader presence and
378 function at Glutamatergic, GABAergic, and Glycinergic synapses. *dlg4a&b*, *gephyrinb*, or *nlgn3b*
379 knockdown approaches likely have larger impacts on OPC activity and influence more OPCs
380 than did disruption of single synaptic receptors from previous studies. In line with our findings,
381 an *in vitro* study found that incubating neuron-glia co-cultures with extracellular domains of
382 Nlgn3 inhibits OPC differentiation and axon wrapping[55]. Interestingly, disruption of the *nlgn3*
383 homologues, *nlgn1* or *nlgn2*, in oligodendrocytes has no effects on the total myelin sheath
384 length[23], suggesting that synaptic disruption at the OPC stage rather than the oligodendrocyte
385 stage affect myelination. Although non-synaptic roles of Nlgn3 have been reported in glia[56], our
386 results suggest a synaptic role of Nlgn3 on OPC development and myelination: close association
387 between Nlgn3 and synapses by IHC and *in vivo* imaging; reduced MAGUK and Gephyrin puncta
388 in OPCs upon *nlgn3b* knockdown; reduced myelination by truncated Nlgn3 that lacks MAGUK
389 and Gephyrin interaction domains. Moreover, the similar effects on myelination from
390 disruptions of *dlg4a&b*, *gephyrinb*, and *nlgn3b* strongly indicate a role of synapses in OPC
391 development and myelination.

392 The signaling pathways downstream of synapse/Ca^{2+} MDs in OPCs remain to be
393 elucidated. Local Ca^{2+} activity might alter the cytoskeleton via Ca^{2+}-dependent kinases[57] or

394 affect lipid raft domains to change local signaling[54]. Notably, focal adhesion kinases (FAKs) can
395 affect cell motility and interactions with other cells and are tightly connected to Ca^{2+} activity[58].
396 FAKs promotes glioma growth downstream of Nlgn3 in response to neuronal activity[3,59], and we
397 find that *nlgn3* disruption leads to impaired OPC differentiation, reduced oligodendrocyte
398 myelination, and abnormal morphology. Therefore, Nlgn3 and FAKs may act downstream of
399 synapses and Ca^{2+} signaling to regulate OPC behavior through cytoskeletal rearrangement.
400 Overall, our *in vivo* study establishes a relationship between neuronal activity, synaptic
401 assembly, and Ca^{2+} activity at neuron-OPC synapses, and reveals their roles in predicting where
402 myelin sheaths form in oligodendrocytes. This model inspires future directions to investigate
403 the pre- and post- synaptic mechanisms underlying neuron-OPC interactions that regulate OPC
404 development and shape myelination.
405

406 **ACKNOWLEDGMENTS**

407 This work was supported by NMSS postdoctoral fellowship FG-1907-34613 (JL), Warren Alpert
408 Distinguished Scholar Award (JL), and NIH/NINDS grant 1R21NS120650 (KRM). We thank
409 Dwight Bergles, Anusha Mishra, Alex Nechiporuk, and members of the Monk lab for discussions
410 and critical reading of the manuscript. We are indebted to Austin Forbes, Tia Perry, and Grace
411 Halsell-Vore for fish care. We thank Rafael Almeida, Paul Brehm, Marc Freeman, Henrique von
412 Gersdorff, Eric Gouaux, David Lyons, Lei Ma, and Teresa Nicolson for reagents and suggestions
413 as well as Fernanda Coelho, Stefanie Kaech Petrie, and the OHSU microscopy core staff for
414 feedback and assistance in imaging. We thank Lori Vaskalis for graphic design.
415

AUTHOR CONTRIBUTIONS

J.L. conceived the project with input from K.R.M. J.L. carried out experiments and data analyses. T.M. generated constructs for *nlgn3a* and *nlgn3b* disruption, GFP-tagged Nlgn3b, and truncated Nlgn3b. T.C. provided key resources prior to their publication. J.L. and K.R.M wrote the manuscript, and all authors edited and approved of the manuscript.

DECLARATION OF INTERESTS

The authors declare no competing interests.

Additional information

Supplementary Information is available for this paper.

Correspondence and requests for materials should be addressed to Jiaxing Li or Kelly Monk.

FIGURE TITLES AND LEGENDS

Fig. 1. Postsynaptic organizers MAGUK/PSD-95 and Gephyrin are present in zebrafish spinal cord OPCs
(a) Top, schematic fish model showing transverse section orientation; bottom, distribution of soma and synapses in spinal cord transverse sections.
(b-c) Representative IHC images of (b) MAGUK and (c) Gephyrin in *Tg(olig1:Kalta4,10xUAS:myrGFP)* spinal cord at 3 dpf. From left, spinal cord sections, 3D-reconstructed regions, and two examples of puncta in OPCs at single planes. Only the postsynaptic puncta that fall within OPC process volumes are shown in 3D-reconstructed images (green spheres) and are indicated with arrowheads in examples. In each example, from left are the merged channels, the OPC channel, and the MAGUK/Gephyrin channel.
(d) Representative images and enlarged regions of FingR.GFP.PSD-95 and FingR.GFP.Gephyrin driven by *olig1* promoter in OPCs. OPC somas are indicated with arrows. The process regions are enlarged in the right panel. The schematic on the left shows FingR.GFP binding to the proteins of interest.
(e) Quantification of puncta number per OPC by IHC (MAGUK and Gephyrin), FingR.GFP (PSD-95 and Gephyrin), and GFP-tagged (PSD-95 and Gephyrin) in the spinal cord. From left, n = 18, 32, 18, 24, 15, and 14 cells from at least 10 fish each condition.

445 All data are represented as mean ± SEM; (e) Kruskal-Wallis test followed by Dunn's multiple comparison
446 test; scale bars 5 µm.
447
448 **Fig. 2. Some but not all MAGUK and Gephyrin puncta in OPCs are associated with other synaptic**
449 **molecules**
450 (a-f) Representative transverse IHC images of (a-c) MAGUK and (d-f) Gephyrin with Synapsin in
451 *Tg(olig1:Kalta4,10xUAS:myrGFP)* spinal cord OPCs at 3 dpf. (a, d) spinal cord sections, (b, e) alignment
452 example with Synapsin, (c, f) no-alignment example with Synapsin. In each example, from left are 3D
453 reconstructed regions, the merged channels, the OPC channel, the MAGUK/Gephyrin channel, and the
454 Synapsin channel. Only the postsynaptic puncta that fall within OPC process volumes are shown in 3D-
455 reconstructed images (green spheres) with aligned synapsin (magenta spheres) and are indicated with
456 arrowheads in other channels.
457 (g) The % of MAGUK and gephyrin puncta in an OPC that align with presynaptic Synapsin in different CNS
458 regions at 3 dpf. FB&MB, forebrain and midbrain; HB, hindbrain; SC, spinal cord. From left, n= 32, 57, 38,
459 33, 16 and 39 cells from at least 10 fish each condition.
460 (h) Representative IHC images of Gephyrin and Glycine receptors (GlyR) in
461 *Tg(olig1:Kalta4,10xUAS:myrGFP)* spinal cord OPCs at 3 dpf. OPC boundaries are indicated in green.
462 Gephyrin puncta either align with GlyR (green arrowheads) or do not (magenta arrowheads).
463 (i) The % of Gephyrin puncta in an OPC that align with GlyR in spinal cord at 3 dpf. n = 12 cells from 7 fish.
464 All data are represented as mean ± SEM; N.S., not significant; (g) Kruskal-Wallis test followed by Dunn's
465 multiple comparison test; scale bars 5 µm.
466
467 **Fig. 3. *In vivo* imaging reveals downregulation of PSD-95-GFP and GFP-Gephyrin upon OPC**
468 **differentiation**
469 (a-b) Representative images of PSD-95-GFP and GFP-Gephyrin (magenta) in spinal cord (a) OPCs and (b)
470 neurons at 3 dpf. Cell membranes indicated with cyan.
471 (c-d) Quantification of (c) PSD-95-GFP and (d) GFP-Gephyrin puncta number in OPCs before and after the
472 last process disappearance, set as time zero, during differentiation. Left, individual traces (grey lines)
473 with the average (black line) and the standard deviation (shade). Right, paired comparison before and
474 after time zero. (c) n= 12 cells from 8 fish; t[11] = 3.922. (d) n= 12 cells from 8 fish; t[11] = 2.705.
475 (e) Representative images of PSD-95-GFP and GFP-Gephyrin (magenta) in differentiating
476 oligodendrocytes (cyan) at 2-3 dpf. Nascent sheaths are indicated with black arrowheads, and processes
477 are indicated with magenta arrowheads.
478 (f) Enrichment of PSD-95-GFP and GFP-Gephyrin puncta in processes and sheaths of differentiating
479 oligodendrocytes. n = 12 and 14 from at least 10 fish each condition.
480 All data are represented as mean ± SEM; N.S., not significant; (c,d) ratio-paired *t*-test; (f) Wilcoxon
481 matched-pairs signed rank test; scale bars 5 µm.
482
483 **Fig. 4. PSD-95-GFP and GFP-Gephyrin puncta in OPCs are dynamic and repeatedly assemble at**
484 **hotspots**
485 (a) Representative *in vivo* images at 2 timepoints of GFP-Gephyrin in a neuron and an OPC next to each
486 other in the spinal cord at 3 dpf, related to Supplementary Video 1.
487 (b) Normalized puncta number per cell of PSD-95-GFP and GFP-Gephyrin in neurons and OPCs within 30
488 minutes. Black line, average; shaded area, standard deviation. From left, n = 12, 3, 4, and 6 cells from 6,
489 10, 4, and 4 fish.
490 (c) Puncta duration in log scale in neurons (N) and OPCs at 3 dpf for PSD-95-GFP, FingR.GFP.PSD-95, GFP-
491 Gephyrin, and FingR.GFP.Gephyrin. n = 13, 5, 6, 7, 4, 7, 5, and 7 cells from at least 4 fish each condition.

492 (d) Convex hull of OPC processes and GFP-Gephyrin puncta over 7 hours. The OPC process convex hull is
493 in magenta and GFP-Gephyrin convex hull is in green. An OPC at a single timepoint is shown on top.
494 (e) Volumes of OPC process convex hull, GFP-Gephyrin puncta convex hull, OPC at a single timepoint,
495 and GFP-Gephyrin hotspots. From left, n= 10, 11, 23, and 18 cells from at least 10 fish.
496 (f-g) Representative time-lapse images of (f) PSD-95-GFP and (g) GFP-Gephyrin within OPC processes.
497 The numbers indicate the corresponding regions. #1 is in a relatively stable process; #2 is in a dynamic
498 process over the imaging time course. The dashed lines outline the process, and arrowheads indicate
499 puncta appearance. Time unit is in minutes.
500 (h-i) Heatmaps of puncta appearance frequency over time for (h) PSD-95-GFP and (i) GFP-Gephyrin. 30%
501 of max frequency is used as coloring threshold: below threshold, grey; above threshold, a shade of
502 magenta corresponding to the frequency. Loci with high puncta appearance frequency (> 3 standard
503 deviations above average) are marked with arrowheads. The numbers with green arrowheads indicate
504 puncta shown in time lapse images in (f-g). Bottom left, image of the OPC with puncta marked with
505 magenta circles.
506 (j) Quantification of loci with high puncta appearance frequency in OPCs. From left, n = 3 and 7 cells
507 from 3 and 5 fish.
508 All data are represented as mean ± SEM; (c,e) Kruskal-Wallis test followed by uncorrected Dunn's
509 multiple comparison test; scale bars 5 µm.
510
511 **Fig. 5. GFP-Gephyrin hotspots in OPCs predict a subset of future myelin sheath formation in a synaptic**
512 **release-mediated manner**
513 (a-b) Representative images of GFP-Gephyrin (green) in an oligodendrocyte lineage cell (magenta) at 2
514 different stages: (a) OPC stage that is 8 hours prior to the onset of myelination and (b) oligodendrocyte
515 stage that is 6 hours after myelination begins, related to Supplementary Video 2.
516 (c) Schematic showing the imaging protocol of individual OPCs that differentiate into myelinating
517 oligodendrocytes (OLs). The first sheath appearance is designated as time 0. Images from up to 10 hours
518 before time 0 are used to identify OPC hotspots, and images after time 0 are used to define sheath
519 regions. TeNT is delivered through ventricle injection before imaging.
520 (d) Single-plane merged image of GFP-Gephyrin puncta frequency heatmap at OPC stage and sheath
521 regions at oligodendrocyte stage. Hotspot regions (black box) and sheaths (yellow) are indicated.
522 Hotspots that exist within where myelin sheaths form are indicated with arrowheads.
523 (e) Frequency distribution of hotspot-sheath (stable) distances with control and TeNT treatments. F[13,
524 168] = 11.39.
525 (f) Quantification of hotspot (Hs)- and nonhotspot (nonHs)-sheath (stable) distances with control and
526 TeNT treatments. control, n = 8 cells from 7 fish; TeNT, n = 6 cells from 6 fish.
527 (g) Percentage of Hs and nonHs in an OPC that predict where myelin sheaths (stable) form within 1 µm
528 with control and TeNT treatments. control, n = 8 cells from 7 fish; TeNT, n = 6 cells from 6 fish.
529 (h) Frequency distribution of Hs-sheath (all) distances with control and TeNT treatments. F[13, 168] =
530 23.69.
531 (i) Quantification of Hs- and nonHs-sheath (all) distances with control and TeNT treatments. control, n =
532 8 cells from 7 fish; TeNT, n = 6 cells from 6 fish.
533 (j) Percentage of Hs and nonHs in an OPC that predict where myelin sheaths (all) form within 1 µm with
534 control and TeNT treatments. control, n = 8 cells from 7 fish; TeNT, n = 6 cells from 6 fish.
535 All data are represented as mean ± SEM; (f,g,i,j) Wilcoxon matched-pairs signed rank test; (e,h) Two-way
536 ANOVA and Fisher's LSD test; scale bars 5 µm.
537
538 **Fig. 6. OPC Ca^{2+} activity is associated with synapses and predicts myelin sheath formation**

539 (a) Representative images of plasma membrane-targeted myrGCaMP6s in an OPC (grey, average
540 projection) showing activity in MDs (cyan).
541 (b) Individual traces plotting myrGCaMP6s intensity ($\Delta F/F_{average}$) in 5 MDs from (a). Scale bar, 100% and
542 50s.
543 (c) Left, the occurrences of Ca^{2+} activity in MDs vs. soma; right, the number of OPCs with only MD
544 activity vs. OPCs with both MD and somal activity. n = 180 cells from 107 fish.
545 (d) Left, representative image of a Ca^{2+} MD (cyan) in an OPC and presynaptic synaptophysin-RFP
546 (magenta); Right, 3-D reconstructed image showing synaptophysin-RFP puncta (magenta) that are
547 within 0.5 µm from MDs (arrowheads).
548 (e) The percentage of Ca^{2+} MDs that are associated with synaptophysin-RFP. n = 7 cells from 7 fish.
549 (f) Time-lapse images of two Ca^{2+} spikes that initiate as puncta and spread to form MDs, indicated by
550 blue arrowheads. The time is in seconds.
551 (g) The two MDs from (f) initiate in proximity (within 0.5 µm) to presynaptic synaptophysin-RFP
552 (magenta), indicated by white arrowheads.
553 (h) Ca^{2+} imaging protocol of individual OPCs that differentiate into oligodendrocytes. The first sheath
554 appearance is designated as time 0. Images up to 6 hours before time 0 are used to identify OPC Ca^{2+}
555 events in MDs, and images around 6 hours after time 0 are used to define sheath regions.
556 (i) Single-plane merged image of Ca^{2+} MDs at OPC stage and sheath regions at oligodendrocyte stage.
557 Ca^{2+} MDs (blue) and sheaths (yellow) are indicated.
558 (j) Quantification of MD- and nonMD-sheath distances. n = 10 cells from 8 fish.
559 (k) Percentage of MDs or nonMDs in an OPC that predict where myelin sheaths form within 1 µm. n = 10
560 cells from 8 fish.
561 All data are represented as mean ± SEM; (j,k) Wilcoxon matched-pairs signed rank test; scale bars 5 µm.
562
563 **Fig. 7. Synaptic release contributes to generating OPC Ca^{2+} activity *in vivo***
564 (a) Schematic showing OPCs neighboring few and many TeNTlc-expressing axons with the sparse-
565 labeling approach.
566 (b) Representative images of OPCs neighboring few (<4) and many (≥4) axons expressing TeNTlc-
567 tdtomato.
568 (c) The frequency of Ca^{2+} activity and peak amplitude in OPCs that neighbor few (<4) and many (≥4)
569 TeNTlc-expressing axons at 5 dpf. Few, n = 14 cells from 8 fish; many, n = 26 cells from 15 fish; t[37] =
570 2.420 and t[38] = 2.958.
571 (d) Experimental paradigm of reagent delivery and Ca^{2+} imaging.
572 (e) Representative single-plane images of individual spinal cord OPCs immediately and 10 min after
573 ventricle injection of $Dextran^{3000}$ Texas Red (magenta) in *Tg(olig1:Kalta4,10xUAS:myrGFP)* animals.
574 (f) Representative images of myrGCaMP6s (grey, average projection) and Ca^{2+} MDs (cyan) with control
575 and TeNT treatment.
576 (g) Normalized Ca^{2+} MD number and frequency of Ca^{2+} activity in OPCs before (blue) and after (magenta)
577 injection of control or TeNT solution at 5 dpf. Paired data are indicated with grey lines. control, n = 17
578 from 13 fish; TeNT, n = 26 cells from 18 fish.
579 (h) Normalized Ca^{2+} MD number and frequency of Ca^{2+} activity in OPCs before (blue) and after (magenta)
580 injection of control or TTX solution at 5 dpf. Paired data are indicated with grey lines. From left, n = 13
581 and 17 cells from 6 and 9 fish.
582 (i) Normalized Ca^{2+} MD number and frequency of Ca^{2+} activity in OPCs before (blue) and after (magenta)
583 injection of control or TTX solution at 3 dpf. Paired data are indicated with grey lines. From left, n = 15
584 and 31, cells from 7 and 13 fish.
585 All data are represented as mean ± SEM; N.S., not significant; (c) unpaired *t*-test or (g,h,i) Wilcoxon
586 matched-pairs signed rank test; scale bars 5 µm.

587
588 **Fig. 8. Disruption of postsynaptic molecules impairs OPC development and myelination.**
589 (a) Representative images of an OPC and an oligodendrocyte in a *nlgn3b*-targeted fish.
590 (b-c) Percentage of oligodendrocytes that myelinate in ctrl-, *dlg4ab*-, *gephyrinb*-, *nlgn3a*-, and *nlgn3b*-
591 targeted fish at (b) 3 dpf and (c) 5 dpf. 3 dpf, n = 144, 57, 49, 41, and 193 cells from 78, 30, 27, 26, and
592 97 fish; 5 dpf, n = 155, 58, 79, 84, and 198 cells from 80, 36, 40, 61, and 93 fish.
593 (d) Representative morphologies of oligodendrocytes with control- (ctrl), *dlg4ab*-, *gephyrinb*-, and
594 *nlgn3b*-targeted for cell-specific knockdown at 3 dpf and 5 dpf.
595 (e) Total length of myelin sheaths per oligodendrocyte at 3 dpf in ctrl-, *dlg4ab*-, *gephyrinb*-, *nlgn3a*-, and
596 *nlgn3b*-targeted oligodendrocytes. n = 121, 50, 34, 30, and 170 cells from 78, 30, 27, 26, and 97 fish.
597 (f) Total length of myelin sheaths per oligodendrocyte at 5 dpf in ctrl-, *dlg4ab*-, *gephyrinb*-, *nlgn3a*-, and
598 *nlgn3b*-targeted oligodendrocytes and mScarlet-, Nlgn3-, Nlgn3 (Δ116)-expressing oligodendrocytes. n =
599 118, 52, 63, 80, 152, 40, 40, and 49 cells from 80, 36, 40, 61, 93, 31, 36, and 39 fish.
600 (g) Morphology of oligodendrocytes with ctrl- and *nlgn3b*-targeted for cell-specific knockdown at 5 dpf.
601 Top, 3D-reconstructed single oligodendrocyte with sheath (colored) and non-sheath (gray). Sheath
602 (black arrowheads) and processes (magenta arrowheads) are indicated.
603 (h) *In vivo* model of neuron-OPC synapses: they are composed of MAGUK and Gephyrin and contribute
604 to OPC Ca^{2+} activity through spontaneous release; they exhibit fast dynamics, which enable OPCs to
605 survey large spatial volumes; synaptic assembly hotspots and associated Ca^{2+} activity at the OPC stage
606 predict where a subset of myelin sheaths form at the oligodendrocyte stage; synaptic assembly is
607 regulated through development while disruption of synaptic molecules impairs OPC development and
608 myelination.
609 All data are represented as mean ± SEM; N.S., not significant; (b,c,e,f) Kruskal-Wallis test followed by
610 uncorrected Dunn's multiple comparisons test; scale bar 5 µm.
611

612

613 **EXTENDED DATA FIGURE TITLES AND LEGENDS**

614 **Extended Data Fig. 1. MAGUK/PSD-95, Gephyrin, and Nlgn3 are present in OPCs, related to Fig. 1**
615 (a) RNA-seq expression of murine *Dlg4* (encodes PSD-95), *Gephyrin*, and *Nlgn3* in different CNS cell
616 types[19]. Micro/Macro, Microglia and Macrophage; NFO, Newly-formed oligodendrocyte; MOL,
617 Myelinating oligodendrocyte.
618 (b) Single cell RNA-seq expression of zebrafish *dlg4* (*a/b*), *gephyrin* (*a/b*), and *nlgn3* (*a/b*)[17]. VLMC,
619 Vascular lepotomeningeal cell; MOL, Myelinating oligodendrocyte.
620 (c) Representative IHC images of PSD-95 in *Tg(olig1:Kalta4,10xUAS:myrGFP)* spinal cord at 3 dpf. From
621 left, spinal cord sections, 3D-reconstructed regions, and two examples of puncta in OPCs at single planes.
622 Only the postsynaptic puncta that fall within OPC process volumes are shown in 3D-reconstructed
623 images (green spheres) and are indicated with arrowheads in examples. In each example, from left are
624 merged channel, OPC channel and PSD-95 channel.
625 (d) % of puncta localized to OPC process (P) and soma (S). MAGUK, n = 18 cells from 8 fish; Gephyrin, n =
626 40 cells from 15 fish.
627 All data are represented as mean ± SEM; scale bars 5 µm.
628
629 **Extended Data Fig. 2. MAGUK and Gephyrin puncta numbers in OPCs increase during early**
630 **development and exhibit small differences across CNS regions, related to Fig. 1**

631 (a) Quantification of MAGUK (green) and Gephyrin (magenta) puncta number per OPC in the spinal cord
632 at different ages by IHC. From left, n = 20, 18, 8, 17, 24, and 8 cells from at least 6 fish per condition.
633 (b) Quantification of MAGUK (green) and Gephyrin (magenta) puncta number per OPC at 3 dpf across
634 different CNS regions. FB&MB, forebrain and midbrain; HB, hindbrain; SC, spinal cord. From left, n = 34,
635 59, 43, 34, 18, and 40 cells from at least 10 fish per condition.
636 (c) Schematic model showing the neuron-rich (NR) and axon & synapse-rich (AR) regions and two
637 representative images showing OPCs with soma localized to NR (top) and AR (bottom) regions in
638 *Tg(olig1:Kalta4,10xUAS:myrGFP)* spinal cord.
639 (d) Quantification of MAGUK (green) and Gephyrin (magenta) puncta number per OPCs in NR or AR
640 regions at 2-3 dpf. From left, n = 14, 5, 15, and 10 cells from at least 5 fish per condition.
641 All data are represented as mean ± SEM; N.S., not significant; (a-b) Kruskal-Wallis test followed by
642 Dunn's multiple comparison test; (d) Mann-Whitney test; scale bar 5 µm.
643
644 **Extended Data Fig. 3. *In vivo* characterization of PSD-95-GFP and GFP-gephyrin, related to Fig. 3 and 4**
645 (a) Puncta diameter of PSD-95-GFP (green) and GFP-Gephyrin (magenta) in spinal cord neurons (N) and
646 OPCs from 2-3 dpf larvae. From left, n = 10, 11, 15, and 29 cells from at least 8 fish per condition.
647 (b-c) Representative *in vivo* images of (b) PSD-95-GFP or (c) GFP-Gephyrin and synaptophysin-RFP (syn.)
648 in spinal cord OPCs at 3 dpf. From left, single plane images and an example of puncta in OPCs at single
649 planes with 3D reconstructed regions, the merged channels, the PSD-95-GFP or GFP-Gephyrin channels,
650 and the syn. channel. In the examples, the alignments are indicated with arrowheads.
651 (d) The % of PSD-95-GFP and GFP-gephyrin puncta in an OPC that align with presynaptic synaptophysin-
652 RFP in the spinal cord in (b-c). n = 13 and 20 cells from at least 10 fish.
653 (e-f) The correlation analysis of puncta number of (e) PSD-95-GFP and (f) GFP-Gephyrin with the
654 corresponding protein overexpression levels at 3 dpf. The linear fit extrapolated to zero overexpression
655 level is at puncta number of 28.6 and 22.9, respectively.
656 (g) Puncta number of PSD-95-GFP (green) and GFP-Gephyrin (magenta) per OPC in the spinal cord at 2
657 dpf and 3 dpf. From left, n = 16, 18, 29, and 14 cells from at least 5 fish per condition.
658 (h) Representative IHC images of PSD-95-GFP in spinal cord OPCs at 3 dpf with GFP (green) and MAGUK
659 (magenta) antibodies. Left, merged channels; middle and right, single channels. Arrowheads indicate the
660 GFP puncta that colocalize with MAGUK signals; cyan arrows indicate the diffused GFP that does not
661 colocalize with MAGUK signals.
662 (i) % of GFP signal that colocalizes with MAGUK signals from (h) using Imaris. n = 4 and 6 fish per
663 condition.
664 All data are represented as mean ± SEM; (a,g) Mann-Whitney test; (e,f) Pearson correlation analysis with
665 linear regression; scale bars 5 µm.
666
667 **Extended Data Fig. 4. Gephyrin hotspots predict a subset of myelin sheath formation in a synaptic**
668 **release-mediated manner, related to Fig. 5**
669 (a) Representative EM image of zebrafish dorsal spinal cord transverse section at 5 dpf[40]. Myelinated
670 axons are indicated with magenta dots.
671 (b) Representative IHC images of zebrafish dorsal spinal cord transverse section at 5 dpf in *Tg(mbp:GFP-*
672 *caax)*. Myelin sheaths that wrap axons form circle structures ("sheath").
673 (c) Quantification of the nearest distance between dorsal myelinated axons from (a) and (b). n = 16 and
674 9 sections from 1 and 6 fish; t[23]=1.627.
675 (d) Schematic showing the puncta inside hotspots (PIH) and the puncta outside hotspots (POH).
676 (e) Percentage of GFP-Gephyrin PIH and POH that predict future myelin sheaths within 1 µm and
677 percentage of stable myelin sheath volume over the entire volume of OPC with control and TeNT
678 treatments.

679 (f) Percentage of future stable myelin sheaths in oligodendrocytes that are predicted by hotspots in
680 OPCs (within 1 µm) with control and TeNT treatments. n = 6 cells from 6 fish.
681 (g) Representative image of individual spinal cord OPCs 50 min after ventricle injection of Dextran^{150,000}
682 Antonia Red (magenta) in *Tg(olig1:Kalta4,10xUAS:myrGcamp6s)* fish.
683 (h-j) Quantification of (h) convex hull volume, (i) hotspot number, and (j) sheath number in control and
684 TeNT treatment conditions. (h) n = 11 and 6 cells from 10 and 6 fish; (i) n = 18 and 6 cells from 16 and 6
685 fish; (j) n = 11 and 6 cells from 10 and 6 fish.
686 (k) Representative time-lapse images of transient ensheathments after time 0 in
687 *Tg(sox10:Kalta4,10xUAS:myrmScarlet)*. Arrowheads indicate the sheath appearances. Time unit is in
688 minutes.
689 (l) Frequency distribution of hotspot-transient ensheathment distances with control and TeNT
690 treatments. F[14, 180] = 23.87.
691 (m) Quantification of Hs- and nonHs-sheath (stable) distances with control and TeNT treatments. control,
692 n = 8 cells from 7 fish; TeNT, n = 6 cells from 6 fish.
693 (n) Percentage of Hs or nonHs in an OPC that predict where transient ensheathments form within 1 µm
694 with control and TeNT treatments. control, n = 8 cells from 7 fish; TeNT n = 6 cells from 6 fish.
695 All data are represented as mean ± SEM; (c) unpaired *t*-test; (e) Friedman test with Dunn's test; (f,h,i,j)
696 Mann-Whitney test; (l) Two-way ANOVA and Fisher's LSD test; (m,n) Wilcoxon matched-pairs signed
697 rank test; scale bars 5 µm.
698
699
700 **Extended Data Fig. 5. The role of synaptic release and neuronal activity in generating OPC Ca^{2+} activity,**
701 **related to Fig. 7**
702 (a) Basal GCaMP6s intensity and MD feret's diameter in OPCs that neighbor few (< 4) and many (≥ 4)
703 TeNTlc-expressing axons at 5 dpf. Few, n = 14 cells from 8 fish; many, n= 26 cells from 15 fish; t[38] =
704 2.375 and t[38] = 2.351.
705 (b) Normalized peak amplitude, peak duration, area of Ca^{2+} MD, basal intensity, and MD Feret's
706 diameter in OPCs before (blue) and after (magenta) injection of control or TeNT solution at 5 dpf. Paired
707 data are indicated with grey lines. Control, n = 17 cells from 13 fish; TeNT, n = 26 cells from 18 fish.
708 (c-d) Normalized peak amplitude, peak duration, and area of Ca^{2+} MD in OPCs before (blue) and after
709 (magenta) injection of control or TTX solution at (c) 5 dpf and (d) 3 dpf. Paired data are indicated with
710 grey lines. From left, n = 15 ,31, 13, and 17 cells from 7, 13, 6, and 9 fish.
711 (e) Representative images of a primary motor neuron visualized by injecting *mnx1:gal4* into
712 *Tg(10xUAS:myrGCaMP6s)*.
713 (f) Normalized frequency of Ca^{2+} activity in motor neurons before (blue) and after (magenta) injection of
714 control or TTX solution at 5 dpf. n = 7 and 6 cells from 5 and 5 fish.
715 All data are represented as mean ± SEM; N.S., not significant; (a) unpaired *t*-test or (b,c,d,f) Wilcoxon
716 matched-pairs signed rank test; scale bars 5 µm.
717
718 **Extended Data Fig. 6. Cell-specific knockdown system is efficient to disrupt genes in oligodendrocytes**
719 **in zebrafish, related to Fig. 8**
720 (a) Schematic of the plasmid (10xUAS:myrmScarlet-p2A-Cas9, U6:sgRNA1;U6:sgRNA2) used to induce
721 cell-specific Cas9 expression with membrane labeling and 2 separate U6-driven sgRNAs.
722 (b) Representative gel images of digested PCR product of genomic regions targeted by the sgRNAs. Each
723 lane represents a single embryo at 1 dpf. The left 4 lanes are uninjected (-) and the right 4 lanes are
724 injected (+) with sgRNAs and Cas9 protein.
725 (c) Schematic of larva with sparsely labeled oligodendrocyte lineage cells resulting from *Tg(sox10:Kalta4)*
726 crossed with transgenic fish carrying the plasmid from (a).

727 (d) Representative images of single oligodendrocytes in the spinal cord of *Tg(10xUAS:myrmScarlet-p2A-*
728 *Cas9, U6:ctrl-sgRNA1;U6:ctrl-sgRNA2)* and *Tg(10xUAS:myrmScarlet-p2A-Cas9, U6:myrf*^{ex3}*-*
729 *sgRNA;U6:myrf*^{ex4}*-sgRNA)* at 6 dpf. Knockdown of Myrf serves as a control for our targeting approach.
730 (e) Average myelin sheath length in (d). n = 24 and 22 cells from 15 fish; t[44] = 2.247.
731 All data are represented as mean ± SEM; N.S., not significant; (e) unpaired *t*-test; scale bars 5 µm.
732
733 **Extended Data Fig. 7. Nlgn3 is localized to synapses and knock-down reduces postsynaptic puncta in**
734 **OPCs, related to Fig. 8**
735 (a) Representative single-plane IHC images of Nlgn3 (Af1010[60]) in OPCs with presynaptic marker SV2 in
736 *Tg(olig1:myrmScarlet)* spinal cord at 5 dpf. From left, spinal cord sections and two alignment examples
737 with SV2. In each example, from left are 3D reconstructed regions, the merged channels, the OPC
738 channel, the Nlgn3 channel, and the SV2 channel. Only the postsynaptic puncta that fall within OPC
739 process volumes are shown in 3D-reconstructed images (green spheres) with aligned SV2 (magenta
740 spheres) and are indicated with arrowheads in other channels.
741 (b) The number of Nlgn3 puncta in an OPC that align with presynaptic SV2 in the spinal cord at 5 dpf
742 from control and F0 larvae with *nlgn3a and nlgn3b* knocked down by sgRNA targeting *nlgn3a*^{ex4} and
743 *nlgn3b*^{ex1} and Cas9 protein. From left, n= 6 and 7 cells from at least 5 fish each condition.
744 (c) Representative *in vivo* images of Nlgn3b-GFP and synaptophysin-RFP (syn.) in the spinal cord of a
745 *Tg(olig1:Kalta4)* larva at 5 dpf. From left, single plane image and two examples of puncta in OPCs at
746 single planes with 3D reconstructed regions, the merged channels, the Nlgn3b-GFP channel, and the syn.
747 channel. In the examples, the aligned Nlgn3b puncta are indicated with arrowheads.
748 (d) Number of Nlgn3b-GFP puncta in OPCs that align with synaptophysin-RFP puncta. n=6 cells from 6
749 fish.
750 (e) Representative IHC images of MAGUK and Gephyrin in *Tg(sox10:Kalta4,10xUAS:myrmScarlet-p2A-*
751 *Cas9)* spinal cord at 3 dpf with ctrl- and *nlgn3b*-targeted for cell-specific knockdown. From left, spinal
752 cord sections and 3D-reconstructed images of enlarged regions. In 3D-reconstructed images, only the
753 postsynaptic puncta that fall within OPC process volume are shown (green sphere).
754 (f) Density of MAGUK and Gephyrin puncta in OPCs from (e). From left, n = 12, 12, 16, and 16 cells from
755 at least 8 fish.
756 (g) Representative *in vivo* images of an OPC expressing the cell-specific knockdown construct in
757 *Tg(olig1:Kalta4, olig1:myrGCaMP6s)* at 4 dpf.
758 (h-i) The frequency of (h) Ca^{2+} activity and (i) MD number in ctrl- and *nlgn3b*-targeted OPCs at 3-4 dpf.
759 ctrl, n = 13 cells from 13 fish; *nlgn3b*, n = 17 cells from 16 fish; t[28] = 2.260 and t[28] = 2.511.
760 All data are represented as mean ± SEM; (b,f) Mann-Whitney test; (h,i) unpaired *t*-test; scale bars 5 µm.
761
762 **Extended Data Fig. 8. Disruption of *nlgn3b* impairs OPC development and myelination, related to Fig.**
763 **8**
764 (a-b) Number of myelin sheaths per oligodendrocyte in ctrl-, *dlg4ab-*, *gephyrinb-*, *nlgn3a-*, and *nlgn3b-*
765 targeted oligodendrocytes at (a) 3 dpf and (b) 5dpf. a, n = 121, 50, 34, 30, and 170 cells from 78, 30, 27,
766 26, and 97 fish; b, n = 118, 52, 63, 80, and 152 cells from 80, 36, 40, 61, and 93 fish.
767 (c) Schematic showing the domains of Nlgn3b and the region mutated in the dominant-negative
768 construct employed in our studies.
769 (d) 4 single planes of a trapezoid-shaped process in an oligodendrocyte in *nlgn3b*-targeted larvae at 5
770 dpf. Myelin sheaths are indicated by black arrowheads and abnormal processes by magenta arrowheads.
771 (e) Percentage of oligodendrocytes that possess both myelin sheath(s) and abnormal processes in ctrl-,
772 *nlgn3a-*, and *nlgn3b*-targeted fish at 5 dpf. n = 119, 84, and 170 cells from 80, 61, and 93 fish, F[6] =
773 13.52.

774 All data are represented as mean ± SEM; N.S., not significant; (a,b,e) Kruskal-Wallis test followed by
775 uncorrected Dunn's multiple comparisons test; scale bars 5 µm.
776
777
778 **SUPPLEMENTARY FIGURES WITH TITLES AND LEGENDS**

779 **Supplementary Fig. 1. Antibody verification in zebrafish for Gephyrin (SS147011) and Nlgn3b (Af1010).**
780 (a) IHC images of Gephyrin in the 5 dpf spinal cord in control (ctrl) and F0 larvae with sgRNA targeting
781 *gephyrina*^{ex2}, *gephyrinb*^{ex7}, or *gephyrina*^{ex2}&*gephyrinb*^{ex7} plus Cas9 protein.
782 (b) Quantification of Gephyrin intensity with ctrl and sgRNA targeting *gephyrina*^{ex2}&*gephyrinb*^{ex7} from (a).
783 n = 5 and 9 fish for control and knockdown, respectively; t[12] = 7.322.
784 (c) Representative transverse spinal cord IHC images of Nlgn3 at 5 dpf in wild-type and F0 larvae with
785 *nlgn3a and nlgn3b* knocked down by sgRNA targeting *nlgn3a*^{ex4} and *nlgn3b*^{ex1} and Cas9 protein.
786 (d) Quantification of Nlgn3 intensity in OPCs from (c). From left, n= 6 and 7 cells from at least 5 fish each
787 condition.
788 All data are represented as mean ± SEM; Mann-Whitney test; scale bars 5 µm.
789
790
791
792 **SUPPLEMENTARY VIDEOS WITH TITLES AND LEGENDS**

793 **Video 1. Time-lapse images of GFP-Gephyrin in an OPC and neuron**
794 Representative video of 10xUAS:GFP-Gephyrin in an OPC and a neuron next to each other in the spinal
795 cord of a *Tg(sox10:Kalta4)* larva at 3 dpf. The video was generated through maximum projection of
796 stacks.
797
798 **Video 2. Time-lapse images of GFP-Gephyrin in a differentiating OPC**
799 Representative video of 10xUAS:GFP-Gephyrin in an OPC that eventually differentiates in the spinal cord
800 of a *Tg(sox10:Kalta4, 10xUAS:myrmScarlet)* larva at 3 dpf. The video was generated through maximum
801 projection of stacks.
802
803 **Video 3. Time-lapse images of myrGCaMP6s in an OPC**
804 Representative video of Ca^{2+} activity in an OPC in a *Tg(olig1:Kalta4,10xUAS:myrGCaMP6s)* larva at 5 dpf.
805
806 **Video 4. Time-lapse images of myrGCaMP6s in an OPC with both MD and somal Ca^{2+} activity**
807 Video of Ca^{2+} activity in an OPC with multiple events including a somal event in a
808 *Tg(olig1:Kalta4,10xUAS:myrGCaMP6s)* larva at 5 dpf.
809
810 **Video 5. Time-lapse images of myrGCaMP6s in an OPC before and after injection of TeNT at 5 dpf**
811 Representative 10-minute video of Ca^{2+} activity in an OPC before (left) and after (right) injection of TeNT
812 in a *Tg(olig1:Kalta4,10xUAS:myrGCaMP6s)* larva at 5 dpf.
813
814 **SUPPLEMENTARY TABLES WITH TITLES AND LEGENDS**

815 **Table 1. A list of primers used in this study**
816

METHODS

RESOURCE AVAILABILITY

Lead contact

Further information and requests for resources and reagents should be directed to and will be fulfilled by the lead contacts, Jiaxing Li (lijia@ohsu.edu) or Kelly Monk (monk@ohsu.edu).

Materials availability

All reagents generated in this paper will be shared by the lead contacts upon request.

Data and code availability

All data reported in this paper will be shared by the lead contacts upon request.

All original code is available from the lead contacts upon request.

Any additional information required to reanalyze the data reported in this paper is available from the lead contacts upon request.

EXPERIMENTAL MODEL AND SUBJECT DETAILS

We used the following existing zebrafish lines and strains: *Tg(sox10:Kalta4)*[61], *Tg(olig1:Kalta4)*[17], *Tg(huc:synaptophysin-RFP)*[17], *Tg(olig2:dsRed)*, *Tg(sox10:GFP-caax)*, *nacre*, and AB. The following lines were newly generated for this study: *Tg(10xUAS:myrGCaMP6s)*, *Tg(olig1:myrGCaMP6s)*, *Tg(10xUAS:myrGFP)*, *Tg(10xUAS:myrmScarlet)*, *Tg(olig1:myrmScarlet)*. All experimental fish were crossed into the *nacre* background for optimal optics without pigmentation. The Kalta4/UAS system allowed sparse labeling and single cell analysis. The genotypes of fish used for each experiment are indicated in figure legends. Animals in the fish facility were maintained at 28° C with a 14 h/10 h light/dark cycle. Larvae and juveniles were nurtured with rotifer

839 suspension and dry food (Gemma 75 and 150, respectively). Adults were fed with a
840 combination of brine shrimp and dry food (Gemma 300). Male and female fish of 3 to 12
841 months-old were mated; larval fish of 2 dpf to 5 dpf were used for experiments (sex is not
842 determined at these stages in zebrafish). All zebrafish experiments and procedures were
843 performed in compliance with institutional ethical regulations for animal testing and research
844 at Oregon Health and Science University (OHSU). Experiments were approved by the
845 Institutional Animal Care and Use Committee of OHSU. Animal and cell numbers are indicated
846 in figure legends.
847

848 **METHOD DETAILS**

849 **Tissue sectioning and immunohistochemistry**

850 To prepare transverse sections, zebrafish larvae at indicated stages were first anesthetized with
851 tricaine and then fixed in 4% PFA, 0.1% Triton at 4° C overnight. Heads and tails were removed
852 to enable better penetration of fixative. The fish were then washed in PBS, 0.1% Triton for 5
853 minutes and passed in 10%, 20%, and 30% sucrose in PBS, followed by OCT embedding and
854 cryosectioning of 20-25 µm slices. The sections were brought to room temperature for 45
855 minutes and rehydrated in PBS, 0.2% Triton for 1 hour. 3% BSA, 5% NGS, 0.2% Triton in PBS was
856 used as blocking buffer. Primary antibodies: chicken anti-GFP (Invitrogen A10262), 1:1000,
857 mouse anti-Pan-MAGUK (NeuroMab K28/86) 1:500, mouse anti-Gephyrin (Synaptic Systems
858 147011) 1:1000, rabbit anti-Synapsin 1/2 (Synaptic Systems 106002) 1:1000, mouse anti PSD-95
859 6G6-1C9 (MAB1596) 1:1000, rabbit anti-Glycine receptor (Synaptic Systems 146008) 1:1000,
860 mouse, anti-SV2 (DSHB AB_2315387) 1:1000, rabbit anti-Nlgn3 (nittobo medical Af1010) 1:1000.

861 The MAGUK antibody was previously validated in zebrafish[62–64], and we validated Gephyrin and
862 Nlgn3 antibody in zebrafish (Supplementary Fig. 1). Secondary antibodies: A488 anti-chicken,
863 A594 anti-rabbit, A647 anti-mouse IgGI, A647 anti-mouse (Thermo Fisher). The stained samples
864 were mounted in prolong Glass (Invitrogen P36980) for at least a day before imaging.

865 **Plasmid construction**

866 In zebrafish, *gephyrin* is duplicated (*gephyrina* and *gephyrinb*), and there are multiple isoforms
867 for both genes. All isoforms are almost identical in protein sequence except for the inclusion or
868 exclusion of C3 and C4 cassettes. We amplified several isoforms from cDNA and decided to
869 follow up two: *gephyrinb* isoform X6 (XM_021468341) because it encodes a protein that is 96%
870 identical and 98% similar to the rat P1 isoform (NP_074056.2)[65] that has been used to track
871 synapses previously; and, *gephyrina* isoform X11 (XM_017351650.2) because it contains a C3
872 cassette previously reported to be present in glia cells[66].

873 Total RNA was extracted from 3 dpf zebrafish AB larvae (50 fish) using RNAeasy Plus Kit
874 (Qiagen 74134). cDNA was synthesized using SuperScript IV Reverse Transcriptase (Invitrogen).
875 Two sets of primers (Supplementary Table 1) were used to clone the full length *gephyrina* and
876 *gephyrinb* using high fidelity Q5 DNA polymerase, followed by A-addition and TA cloning into
877 pCRII-TOPO backbones. Using Gibson assembly (NEB E5510S), we added EGFP to the 5' end and
878 a linker GGGGSGGGGSGGGGS in between, and integrated it into pCS 2.1 backbones with an
879 AVRII digestion site. The 5' end was chosen based on previous imaging studies[65]. In transient
880 injections, GFP-Gephyrina and GFP-Gephyrinb exhibited similar expression profiles; therefore,
881 we used GFP-Gephyrinb for our studies and refer to the GFP-3xGGGGS-Gephyrinb as GFP-
882 Gephyrin throughout the manuscript. Using Gateway BP reaction (Invitrogen 11786100), we

883 generated pME_ATG-GFP-Gephyrinb. Using AVRII and KPNI-HF, we cut GFP-Gephyrinb (without
884 an ATG) from the pCS 2.1 backbone and inserted it in frame into p3E_p2A to generate
885 p3E_p2A-GFP-Gephyrinb.

886 *PSD-95/dlg4b* transcript NM_214728.1 encodes a protein that is 76% identical and 83%
887 similar to rat *Dlg4* (NP_062567.1) and was thus chosen for use in our studies. We added GFP to
888 the 3'end because N-terminal palmitoylation of PSD-95 is necessary for its synaptic localization,
889 and receptor clustering[67,68]. It was cloned from cDNA with primers (Supplementary Table 1)
890 similar to *gephyrin* as described above. We refer to PSD-95-3xGGGGS-GFP as PSD-95-GFP. We
891 generated pME_ATG-PSD-95-GFP and p3E_p2A-PSD-95-GFP constructs.

892 *nlgn3b* transcript XM_005165182 encodes a protein that is 72% identical and 81%
893 similar to mouse *Nlgn3* (NP_766520). We synthesized the coding region from XM_005165182
894 using IDT Gene Synthesis. For GFP-labeling, we inserted GFP at 3' end with a linker and
895 generated pME_Nlgn3-GFP. In addition, we generated pME_Nlgn3 (full length) and pME_Nlgn3
896 (Δ116) that misses both domains for interactions with MAGUK and Gephyrin[23,46].

897 pCAG_FingR.GFP-Gephyrin-CCR5TC (Addgene 46296) and pCAG_FingR.GFP-PSD-95-
898 CCR5TC (Addgene 46295) were used to amplify the coding region with additional 5' zinc finger
899 binding sequence to regulate their expression[20], followed by BP reaction to generate
900 pME_zincfinger_FingR.GFP-PSD-95-CCR5TC and pME_zincfinger_FingR.GFP-Gephyrin-CCR5TC
901 constructs.

902 pME_myrGFP, pME_myrmScarlet and pME_myrRFP-T were generated using PCR and BP
903 reaction, using Fyn myristoylation and palmitoylation domain. p3E_mScarletcaax was
904 generated using PCR and BP reaction. pGP-CMV-GCaMP6s[69] (Addgene 40753) was used as a

905 template and 3 primers were used in a Q5 PCR (15 cycles at 71° C and 20 cycles at 72° C) to
906 amplify GCaMP6s and add a Kozak sequence, myr (Fyn myristoylation and palmitoylation
907 domain), attB1, and attB2 sequences. This PCR product was used to generate
908 pME_myrGCaMP6s using BP reaction.

909 We obtained multiple plasmids from Tol2 kits: pDestTol2pA2, pDONR221, p5E_10xUAS,
910 p3E_polyA, p3E_p2A[70], p5E_sox10$_{7.2kb}$[61], pDestTol2pACryGFP (pDestTol2GE),
911 pDestTol2pACrymCherry (pDestTol2RE).

912 Using Gateway LR reactions (Invitrogen 11791020), we generated the following
913 constructs: GE-10xUAS:myrEGFP, RE-10xUAS:myrmScarlet, PA2-olig1:myrmScarlet, GE-
914 10xUAS:myrGCaMP6s, PA2-olig1:myrGCaMP6s, GE-10xUAS:GFP-Gephyrinb, RE-10xUAS:GFP-
915 Gephyrina, GE-10xUAS:PSD-95-GFP, PA2-sox10:myrRFP-T-P2A-GFP-Gephyrinb, PA2-
916 sox10:myrRFP-T-P2A-PSD95-GFP, GE-10xUAS:zincfinger_FingR.GFP-PSD-95-CCR5TC, GE-
917 10xUAS:zincfinger_FingR.GFP-Gephyrin-CCR5TC, GE-10xUAS:Nlgn3b-GFP, RE-10xUAS:Nlgn3-
918 P2A-mScarletcaax, RE-10xUAS:Nlgn3(Δ116)-P2A-mScarletcaax. We used Mnx1:Gal4[71] to drive
919 myrGCaMP6s expression in motor neurons. We used Huc:Kalta4 [61], UAS:TeNTlc-tdtomato[45] to
920 drive TeNTlc expression in neurons. All constructs generated in this study were fully sequenced
921 (except *sox10* and *olig1* promoters).

922 **Cell specific CRISPR/Cas9 plasmid construction and CRISPR/Cas9-mediated gene disruption**

923 We used 5xUAS:hsp70promoter-Cas9-T2A-GFP, U6:sgRNA1;U6:sgRNA2[72] (Addgene 74009) as a
924 backbone and performed the following modifications: replacement of the 5xUAS:hsp70
925 promoter with the 10xUAS:E1b-bactin-Kozak promoter because we found the original promoter
926 expressed in many non-specific cell types when injected into *Tg(sox10:Kalta4)*; replacement of

927 T2A-GFP with myrmScarlet-p2A and added to the 5'end of Cas9; addition of polyA to the 3' end
928 of Cas9. Four sets of primers and 2 previously made plasmids (Tol2-10xUAS:E1b-mScarlet and
929 Tol2-10xUAS:cas9-P2A-RFPT-caax) were used to generate 4 segments. These segments were
930 integrated into the backbone by NEBuilder HiFi assembly (NEB E2621S). The new construct is
931 referred to as 10xUAS:myrmScarlet-p2A-Cas9, U6:sgRNA1;U6:sgRNA2.
932 CHOPCHOP and Crisprscan were used to identify sgRNA sequences for each gene of
933 interest: *dlg4a* exon 6, GGTGACCCACAGTCAGGCGGTGG; *dlg4b* exon 8,
934 GGAAGCAGGACCGATCGTCCGG; *gephyrina* exon 2, GGTCATGAACGAGATCTTTGAGG; *gephyrinb*
935 exon 7, GGAGAGCCGGCAGGATGAACTGG; *gephyrinb* exon 8, GGGCGTCCAGGTTCTTCCGCGGG;
936 *myrf* exon 3, GACCCAACGGCGGTGCACCCGGG; *myrf* exon 4, GCTGGAGTCCGGAGGAGACTCGG;
937 *nlgn3a* exon 1, GGTGTATGATGCTTGTCCGGGGG; *nlgn3a* exon 4, GCCTTGTGTACTTAACCGGCTGG;
938 *nlgn3b* exon 1, GATGCGGGTCGCTGTTGCCACGG; *nlgn3b* exon 3,
939 GGTAGTGTGCTGGCCAGCTACGG. The cutting efficiencies of these sgRNAs were verified (>95%)
940 via enzyme digestion of the targeted locus PCR product (CRISPRtest primers, Extended Data Fig.
941 6b). F0 larvae with *gephyrina* and *gephyrinb* sgRNA injected together with 1 ng Cas9 protein
942 were used to examine the specificity of the Gephyrin antibody. *gephyrinb* disruption was
943 sufficient to eliminate Gephyrin protein in the CNS (Supplementary Fig. 1a-b). BsaI and BsmBI
944 were used to insert the sgRNA into 10xUAS:myrmScarlet-p2A-Cas9, U6:sgRNA1;U6:sgRNA2,
945 while the uninserted plasmid was used as controls. The offspring larvae with sparsely labeled
946 oligodendrocyte were examined for morphology and sheath characteristics.
947 **Sparse labeling and generation of transgenic lines**

948 Fertilized zebrafish eggs at the 1-cell stage were microinjected with 1 nL of an injection
949 solution containing 20 ng/µL plasmid DNA, 25 ng/µL Tol2 transposase mRNA, 0.02% phenol
950 red and 0.2M KCl. Injected F0 animals were either used for single-cell analysis or raised to
951 adulthood to generate transgenic lines. To generate stable lines, F1 progenies were screened
952 for germline transmission of the fluorescent reporters. F1 animals were further outcrossed and
953 maintained in the *nacre* background to establish stable transgenic lines with single copy
954 insertion.

955 **Mounting larvae for *in vivo* imaging**

956 For most live imaging experiments, larvae were anesthetized with 0.16 mg/mL (600 µM)
957 tricaine in embryo medium. The fish were mounted in 0.8% low melting agarose (Sigma A9414)
958 on a coverslip for morphology and sheath examination or in 1.5% low melting agarose in a dish
959 for time lapse imaging (hours). For Gephyrin hotspot and myrGCaMP6s imaging, larvae were
960 immobilized with 0.5 mg/ml non-depolarizing acetylcholine receptor antagonist mivacurium
961 chloride (Abcam) and mounted in 1.5% low melting agarose in a dish.

962 **Confocal microscopy**

963 All imaging was performed on an upright Zeiss LSM 980 confocal with Airyscan 2 in 4Y fast
964 mode. For fixed tissues, a 63x/1.4 NA oil objective was used, and for live imaging, a 20x/1.0 NA
965 water objective was used. All images were taken in Zeiss software. We used the following lasers:
966 488 nm for EGFP, myrGCaMP6s, and Alexa488; 561 nm for RFP, mScarlet, tdtomato, and
967 Alexa594; 639 nm for Alexa647. Fixed tissue was imaged with 0.15 µm z spacing with 1.6x to
968 2.5x zoom. For *in vivo* analyses, PSD-95-GFP and GFP-Gephyrin were imaged with 2 µm z-
969 spacing at an interval of 5 min (for 30 min to 1 hour) or 20 min (for longer than 1 hour) at a

970 zoom between 3.7x-10x depending on OPC cell size. myrGCaMP6s was imaged with 2 µm z-
971 spacing at 0.5 Hz (4 planes scanned) for 10 min or 20 min (drug injection experiments) as
972 previously described[17,18]. Images acquired at 0.5 Hz were analyzed along with images acquired
973 at 10 Hz with a single plane. No major differences were found on the Ca^{2+} spike characteristics,
974 but 0.5 Hz acquisition allowed inclusion of more stacks and increased the number of events
975 detected. Therefore, 0.5 Hz was used throughout the study. For tracking OPCs that differentiate
976 into myelinating oligodendrocyte, Ca^{2+} imaging was done repeatedly for 5 min at the beginning
977 of each hour.

978 **Drug delivery through ventricle injection**

979 For myrGCaMP6s experiments involving drug delivery, we injected drugs via ventricle injection
980 as described previously[18]. In TTX treatment, following 10 min GCaMP6s imaging, a 1 nL mixture
981 containing 0.2M KCL, 0.5% Dextran Texas Red 3000 MW (Thermo), and H_2O (control) or TTX
982 (0.5 mM, kind gift from Henrique von Gersdorff's lab) were pressure injected into the hindbrain
983 ventricle using an ASI MPPI-3. Between 15 and 35 min after injection, Dextran was imaged,
984 followed by another 10 min of GCaMP6s imaging. Dextran surrounding the imaged OPCs was
985 used to verify the drug delivery. TTX caused fish paralysis, further verifying efficient delivery of
986 active drugs. After imaging, fish were removed from mounting media. Larvae injected with
987 control solution recovered full swimming activity within 3 minutes, and TTX-injected paralyzed
988 larvae maintained normal heartbeats for at least 3 hours. In TeNT treatment, an 8 nL mixture
989 containing 0.2M KCL, 0.5% Dextran Antonia Red 150,000 MW (Sigma), and TeNT (listlabs 190A,
990 0.5 µM) were pressure injected into the hindbrain ventricle. Between 50 and 70 min after

991 injection, Dextran was imaged, followed by another 10 min of GCaMP6s imaging. TeNT-injected
992 larvae showed reduced swimming activity.
993
994 **QUANTIFICATION AND STATISTICAL ANALYSIS**
995 **OPC labeling during development**
996 We used *sox10* and *olig1* to label OPCs. *sox10* drives expression in both OPCs and myelinating
997 oligodendrocytes while *olig1* labels only OPCs. OPCs and myelinating oligodendrocytes could be
998 distinguished by cell morphology: OPCs only possessed processes and myelinating
999 oligodendrocytes possessed sheaths. Animal ages and corresponding OPC activity: 2 dpf (when
1000 OPCs are born, and migrate), 3 dpf (when many OPCs initiate differentiation), 5 dpf (when
1001 many OPCs complete differentiation.)
1002 **Alignment rate and colocalization ratio**
1003 Images of fixed tissue were analyzed in Imaris. "Surface" function was used to create a cell
1004 surface (Smooth and Surface Grain Size = 0.0850 µm; Diameter of Largest Sphere = 5 µm;
1005 Threshold between 900-1200; Number of Voxels above 100). "Spot" function was used to
1006 generate $Spot_{postsynaptic\ puncta}$ (Estimated XY Diameter = 0.35 µm; Estimated Z Diameter = 0.5 µm;
1007 Background subtraction; quality above 2500 to 2800). Then the cell surface was used as a mask
1008 to generate $Spot_{postsynaptic\ puncta\ in\ OPCs}$, which was further verified by crosschecking its overlap
1009 with $Spot_{postsynaptic\ puncta}$. $Spot_{postsynaptic\ puncta\ in\ OPCs}$ was analyzed for puncta number or density. To
1010 examine the alignment of MAGUK (Gephyrin) and Synapsin, we used "Spot" function to
1011 generate $Spot_{Synapsin\ puncta}$. By determining the proximity $Spot_{postsynaptic\ puncta\ in\ OPCs}$ to $Spot_{Synapsin}$

1012 puncta using MATLAB-enabled "Colocalize Spots" function (<0.1 µm), we could identify
1013 postsynaptic puncta in OPCs that aligned with Synapsin and calculate the alignment rate.
1014 For colocalization of PSD-95-GFP (or GFP-Gephyrin) and MAGUK (or Gephyrin) antibody
1015 staining, "Surface" function was used to create a GFP surface (Smooth and Surface Grain Size =
1016 0.0850 µm; Diameter of Largest Sphere = 6.5 µm; Threshold between 10000-20000; Number of
1017 Voxels above 100). We used the Imaris "Coloc" function to generate a coloc channel based on
1018 the overlapping pixels between GFP and MAGUK (Gephyrin) channel and generated a coloc
1019 surface (Smooth and Surface Grain Size = 0.0850 µm; Diameter of Largest Sphere = 6.5 µm;
1020 Threshold between 3000-12000; Number of Voxels above 100). We calculated the % of GFP
1021 that colocalize with antibody staining by dividing the coloc surface volume by the GFP surface
1022 volume.
1023 **Postsynaptic puncta identification and analysis from *in vivo* imaging**
1024 Live Images of PSD-95-GFP and GFP-Gephyrin were processed in ImageJ, and synaptic puncta
1025 were identified and tracked with Trackmate[73]. In Trackmate, parameters were set as follows:
1026 LOG mode, diameter 0.75 µm, Quality>100, contrast>0.19 and signal noise >0.35, LAP linking
1027 with 0.5 µm distance and 2 max gap frames allowed were applied. The identified puncta at each
1028 frame were then manually examined to remove poor quality tracks. Neighboring puncta may
1029 sometimes be incorrectly linked between timelapses; therefore, manual examinations were
1030 done to fix these link errors. The data output was analyzed in MATLAB with custom scripts to
1031 calculate puncta number per cell at each timepoint, puncta duration and diameter. To generate
1032 figures of mean and standard deviation as shade, we used a modified script
1033 (https://www.mathworks.com/matlabcentral/fileexchange/29534-stdshade). To analyze the

1034 puncta number during OPC differentiation, it was designated as time 0 when myelinating
1035 oligodendrocyte's last process disappeared and all process transformed into sheaths. In
1036 MATLAB, this information is used to divide the puncta number into before and after time 0 for
1037 each cell. The traces were generated and realigned based on time 0. To analyze the enrichment
1038 of puncta in differentiating oligodendrocytes, the puncta number in sheaths and processes
1039 were divided by the corresponding areas and normalized.

1040 **Hotspot analysis**

1041 Heatmaps of puncta over time were generated using the output data with Heatscatter
1042 (https://www.mathworks.com/matlabcentral/fileexchange/47165-heatscatter-plot-for-
1043 variables-x-and-y). With a sampling volume of 1 x 1 x 4 µm, regions with frequency higher than
1044 three standard deviations were identified as hotspots using custom MATLAB scripts, which also
1045 measured the distance between the center of hotspots and future sheaths. The same set of
1046 puncta were used to generate the convex hull for GFP-Gephyrin. In time-lapse imaging that
1047 encompassed both OPC and oligodendrocyte stages, we used the first nascent sheath
1048 appearance (time 0) to separate OPC stage and oligodendrocyte stage. It takes up to 5 hours for
1049 an oligodendrocyte to complete differentiation[36]; therefore, we identified where sheaths
1050 formed approximately 6 hours after time 0. We grouped the GFP-Gephyrin puncta into the ones
1051 in hotspot regions (PIH) and outside hotspot regions (POH). To choose 30 representative points
1052 outside hotspots in an OPC, we used Trackmate to convert OPC processes to points and
1053 clustered the points outside hotspot regions into 30 groups (nonhotspots) using Lloyd's
1054 algorithm in MATLAB. The same set of points were used to generate the convex hull for OPC
1055 processes.

1056 The distances between an object (hotspots, nonhotspots, PIH, and POH) and myelin
1057 sheaths were measured using custom MATLAB scripts. To examine how such a spot predicted
1058 myelin sheaths, we analyzed the frequency distribution of spot-sheath distances, and calculated
1059 the percentage of distances that were less than 1 µm. To control for the myelin sheath
1060 prediction by GFP-Gephyrin puncta, We calculated the percentage of these puncta that were
1061 within 1 µm from myelin sheaths. In comparison, we calculated the random chance by dividing
1062 the volume occupied by myelin sheaths by the entire volume occupied by OPCs prior to
1063 differentiation. To estimate the myelin sheath volume, the sheath length and width were
1064 measured and the volume was calculated as pi*length*$(width/2)^2$. To estimate the OPC volume
1065 over time, we calculated the volume of the shape generated from process-converted points
1066 using Delaunay triangulation.

1067 **Ca^{2+} events analysis**

1068 myrGCaMP6s images of z-stacks were maximum projected and stabilized using "Image
1069 Stabilizer." The images were assigned with random names using "blindr"
1070 (https://github.com/U8NWXD/blindr) before analysis and reassigned with the original names
1071 after analysis. The regions of Ca^{2+} events (ROI) were identified by "GECIquant"[74] first and then
1072 manually examined frame by frame. The intensity and area of each ROI were exported and
1073 processed in MATLAB through custom scripts. Briefly, $\Delta F/F_{average}$ ($\Delta F=F- F_{average}$) was calculated
1074 to generate traces and to identify intensity peaks using "findpeaks" in MATLAB with filtering
1075 parameters (3 standard deviations above average, prominence larger than 40% of the baseline,
1076 and peak area larger than 2.5). Rare elevated Ca^{2+} signal for extended periods of time (longer
1077 than 50 seconds) were excluded. Peaks were manually verified against the image. Several Ca^{2+}

1078 characteristics were measured: peak amplitude, peak duration, Ca^{2+} MD number, Ca^{2+} MD area,
1079 and frequency of Ca^{2+} activity. A region with multiple OPCs was analyzed for TeNTlc and TeNT
1080 experiment, while single OPCs were analyzed for the rest of experiments. To examine the
1081 proximity of synaptophysin-RFP to Ca^{2+} MD, Ca^{2+} MDs were identified as above, and their
1082 locations were first compared to synaptophysin-RFP manually plane by plane and then verified
1083 by Imaris. In Imaris, using "Spot" and "Surface" functions, we generated synaptophysin-RFP
1084 puncta and OPC surface, with which we identified the puncta that were close to OPC surfaces
1085 using a MATLAB-enabled "Spot-to-Surface" function (0.5 µm threshold). These puncta were
1086 manually checked against Ca^{2+} MDs identified through morphological landmarks in Imaris. The
1087 distance between Ca^{2+} and future sheaths were measured in MATLAB. In TeNTlc experiments,
1088 the number of axons expressing TeNTlc-tdtomato was counted in each image. If the number
1089 was less than 4, the corresponding image was grouped as "neighboring few TeNTlc axons";
1090 otherwise, the image was grouped as "neighboring many TeNTlc axons". The distances between
1091 Ca^{2+} MDs and future myelin sheaths were measured using custom MATLAB scripts. To choose
1092 30 representative points outside MDs in an OPC, we used Trackmate to convert OPC processes
1093 to points and clustered the points outside MD regions into 30 groups (nonMD) using Lloyd's
1094 algorithm in MATLAB. To examine how MDs or nonMDs predicted myelin sheaths, we analyzed
1095 the frequency distribution of MD-sheath and nonMD-sheath distances, and calculated the
1096 percentage of distances that were less than 1 µm. To examine the Ca^{2+} activity in cell-specific
1097 knockdown targeted OPCs, we refined MDs to the mScarlet-labeled processes in order to
1098 analyze only the targeted cells.

1099 **Oligodendrocyte and myelin sheath analysis**

1100 To analyze myelin sheath length and number, we used ImageJ ROI manager to trace all sheaths
1101 of sparsely labeled oligodendrocytes between segments 1 and 15 in spinal cord. The number of
1102 oligodendrocytes analyzed per fish was limited to 3 to ensure even weight among individual fish.
1103 Sheath traces and the corresponding images were blinded using "File Name Encrypter" in
1104 ImageJ. The sheath length and number were then analyzed in MATLAB with custom scripts and
1105 matched with the original genotype following analysis. To calculate the myelinating
1106 oligodendrocyte %, in each imaging experiment, the number of oligodendrocytes from one
1107 genotype was counted and divided to the total number of cells (both oligodendrocytes and
1108 OPCs). In measuring hotspot-sheath distances, we identified the stable myelin sheaths
1109 approximately 6 hours after time 0 when processes without terminal sheaths disappeared and
1110 all sheaths of oligodendrocytes formed. The transient sheaths were identified similarly to a
1111 previous study[47]: larger than 1.5 µm in length and 200% wider than the connected processes. In
1112 order to measure the nearest distance between dorsal myelinated axons with EM and IHC
1113 images, the center of these axons were identified and a nearest point search was performed
1114 using a customized MATLAB script.

1115 **Statistics**

1116 Most data are shown as mean±SEM., with individual data points shown as circles. We
1117 conducted Shapiro-Wilk's test and Levene's test to verify data normality and homoscedasticity,
1118 respectively, before performing two-sided *t*-test for unpaired groups, paired or ratio-paired *t*-
1119 test for paired groups, and one-way ANOVA test for more than 3 groups. If the data did not
1120 pass normality tests, we used Mann-Whitney test for unpaired groups, Wilcoxon matched-pairs
1121 signed rank test for paired groups, Friedman test for repeated measures of more than 3 groups,

1122 and Kruskal-Wallis test for more than 3 groups. These analyses were performed either in
1123 GraphPad Prism or MATLAB. The significance and statistical analyses employed were indicated
1124 in figure legends. Animal and cell number used for each experiment, t-values and df for *t*-tests,
1125 and *F* values and df for ANOVA were indicated in figure legends. Data collection was not
1126 performed blindly due to the experimental conditions, but analyses were performed blindly as
1127 indicated. Sample size was chosen based on standard deviation and effect
1128 (http://www.biomath.info/power/ttest.htm). Sex is not yet determined in zebrafish at the ages
1129 employed in our study and so cannot be considered as a biological variable.
1130

1131 **Reporting summary**

1132 Further information on research design is available in the Nature Research Reporting Summary
1133 linked to this manuscript.
1134

1135 **Data availability**

1136 All research materials are available upon request. Source data are provided with this paper.
1137

1138 **Code availability**

1139 All custom scripts are available upon request.
1140

1141 ## REFERENCES

1142 1. Franklin, R. J. M. & Ffrench-Constant, C. Remyelination in the CNS: From biology to
1143 therapy. *Nature Reviews Neuroscience* vol. 9 839–855 at

1144 https://doi.org/10.1038/nrn2480 (2008).

1145 2. Xiao, Y., Petrucco, L., Hoodless, L. J., Portugues, R. & Czopka, T. Oligodendrocyte
1146 precursor cells sculpt the visual system by regulating axonal remodeling. *Nat. Neurosci.*
1147 **25**, 280–284 (2022).

1148 3. Venkatesh, H. S. *et al.* Targeting neuronal activity-regulated neuroligin-3 dependency in
1149 high-grade glioma. *Nature* **549**, 533–537 (2017).

1150 4. Bergles, D. E. & Richardson, W. D. Oligodendrocyte development and plasticity. *Cold*
1151 *Spring Harb. Perspect. Biol.* **8**, a020453 (2016).

1152 5. Lundgaard, I. *et al.* Neuregulin and BDNF Induce a Switch to NMDA Receptor-Dependent
1153 Myelination by Oligodendrocytes. *PLoS Biol.* **11**, (2013).

1154 6. de Biase, L. M. *et al.* NMDA receptor signaling in oligodendrocyte progenitors is not
1155 required for oligodendrogenesis and myelination. *J. Neurosci.* **31**, 12650–12662 (2011).

1156 7. Zonouzi, M. *et al.* GABAergic regulation of cerebellar NG2 cell development is altered in
1157 perinatal white matter injury. *Nat. Neurosci.* **18**, 674–682 (2015).

1158 8. Balia, M., Benamer, N. & Angulo, M. C. A specific GABAergic synapse onto
1159 oligodendrocyte precursors does not regulate cortical oligodendrogenesis. *Glia* **65**, 1821–
1160 1832 (2017).

1161 9. Mitew, S. *et al.* Pharmacogenetic stimulation of neuronal activity increases myelination
1162 in an axon-specific manner. *Nat. Commun.* **9**, 306 (2018).

1163 10. Hines, J. H., Ravanelli, A. M., Schwindt, R., Scott, E. K. & Appel, B. Neuronal activity biases
1164 axon selection for myelination in vivo. *Nat. Neurosci.* **18**, 683–689 (2015).

1165 11. Gibson, E. M. *et al.* Neuronal activity promotes oligodendrogenesis and adaptive

1166 myelination in the mammalian brain. *Science (80-.).* **344**, (2014).

1167 12. Mensch, S. *et al.* Synaptic vesicle release regulates myelin sheath number of individual

1168 oligodendrocytes in vivo. *Nat. Neurosci.* **18**, 628–630 (2015).

1169 13. Nagy, B., Hovhannisyan, A., Barzan, R., Chen, T. J. & Kukley, M. Different patterns of

1170 neuronal activity trigger distinct responses of oligodendrocyte precursor cells in the

1171 corpus callosum. *PLoS Biol.* **15**, (2017).

1172 14. Barron, T. & Kim, J. H. Neuronal input triggers Ca2+ influx through AMPA receptors and

1173 voltage-gated Ca2+ channels in oligodendrocytes. *Glia* **67**, 1922–1932 (2019).

1174 15. Sun, W., Matthews, E. A., Nicolas, V., Schoch, S. & Dietrich, D. Ng2 glial cells integrate

1175 synaptic input in global and dendritic calcium signals. *Elife* **5**, (2016).

1176 16. Hamilton, N., Vayro, S., Wigley, R. & Butt, A. M. Axons and astrocytes release ATP and

1177 glutamate to evoke calcium signals in NG2-glia. *Glia* **58**, 66–79 (2010).

1178 17. Marisca, R. *et al.* Functionally distinct subgroups of oligodendrocyte precursor cells

1179 integrate neural activity and execute myelin formation. *Nat. Neurosci.* **23**, 363–374

1180 (2020).

1181 18. Krasnow, A. M., Ford, M. C., Valdivia, L. E., Wilson, S. W. & Attwell, D. Regulation of

1182 developing myelin sheath elongation by oligodendrocyte calcium transients in vivo. *Nat.*

1183 *Neurosci.* **21**, 24–30 (2018).

1184 19. Zhang, Y. *et al.* An RNA-sequencing transcriptome and splicing database of glia, neurons,

1185 and vascular cells of the cerebral cortex. *J. Neurosci.* **34**, 11929–11947 (2014).

1186 20. Gross, G. G. *et al.* Recombinant Probes for Visualizing Endogenous Synaptic Proteins in

1187 Living Neurons. *Neuron* **78**, 971–985 (2013).

1188 21. Uezu, A. *et al.* Identification of an elaborate complex mediating postsynaptic inhibition.
1189 *Science (80-.).* **353**, 1123–1129 (2016).
1190 22. Dempsey, W. P. *et al.* Regional synapse gain and loss accompany memory formation in
1191 larval zebrafish. *Proc. Natl. Acad. Sci. U. S. A.* **119**, (2022).
1192 23. Hughes, A. N. & Appel, B. Oligodendrocytes express synaptic proteins that modulate
1193 myelin sheath formation. *Nat. Commun.* **10**, (2019).
1194 24. Marques, S. *et al.* Oligodendrocyte heterogeneity in the mouse juvenile and adult central
1195 nervous system. *Science (80-.).* **352**, 1326–1329 (2016).
1196 25. Spitzer, S. O. *et al.* Oligodendrocyte Progenitor Cells Become Regionally Diverse and
1197 Heterogeneous with Age. *Neuron* **101**, 459-471.e5 (2019).
1198 26. Yoshii, A. & Constantine-Paton, M. BDNF induces transport of PSD-95 to dendrites
1199 through PI3K-AKT signaling after NMDA receptor activation. *Nat. Neurosci.* **10**, 702–711
1200 (2007).
1201 27. Meier, J. & Grantyn, R. A Gephyrin-Related Mechanism Restraining Glycine Receptor
1202 Anchoring at GABAergic Synapses. *J. Neurosci.* **24**, 1398–1405 (2004).
1203 28. El-Husseini, A. E.-D., Schnell, E., Chetkovich, D. M., Nicoll, R. A. & Bredt, D. S. PSD-95
1204 Involvement in Maturation of Excitatory Synapses. *Science (80-.).* **290**, 1364–1368 (2000).
1205 29. Prange, O., Wong, T. P., Gerrow, K., Wang, Y. T. & El-Husseini, A. A balance between
1206 excitatory and inhibitory synapses is controlled by PSD-95 and neuroligin. *Proc. Natl.*
1207 *Acad. Sci. U. S. A.* **101**, 13915–13920 (2004).
1208 30. Saiyed, T. *et al.* Molecular basis of gephyrin clustering at inhibitory synapses: Role of G-
1209 and E-domain interactions. *J. Biol. Chem.* **282**, 5625–5632 (2007).

1210 31. Dejanovic, B. *et al.* Palmitoylation of Gephyrin Controls Receptor Clustering and Plasticity
1211 of GABAergic Synapses. *PLoS Biol.* **12**, 1–16 (2014).
1212 32. Oh, W. C., Lutzu, S., Castillo, P. E. & Kwon, H. B. De novo synaptogenesis induced by
1213 GABA in the developing mouse cortex. *Science (80-.).* **353**, 1037–1040 (2016).
1214 33. Fortin, D. A. *et al.* Live imaging of endogenous PSD-95 using ENABLED: A conditional
1215 strategy to fluorescently label endogenous proteins. *J. Neurosci.* **34**, 16698–16712 (2014).
1216 34. Fang, H., Bygrave, A. M., Roth, R. H., Johnson, R. C. & Huganir, R. L. An optimized
1217 crispr/cas9 approach for precise genome editing in neurons. *Elife* **10**, (2021).
1218 35. Ifrim, M. F., Janusz-Kaminska, A. & Bassell, G. J. Development of single-molecule
1219 ubiquitination mediated fluorescence complementation to visualize protein
1220 ubiquitination dynamics in dendrites. *Cell Rep.* **41**, 111658 (2022).
1221 36. Czopka, T., ffrench-Constant, C. & Lyons, D. A. Individual oligodendrocytes have only a
1222 few hours in which to generate new myelin sheaths invivo. *Dev. Cell* **25**, 599–609 (2013).
1223 37. Almeida, A. R. & Macklin, W. B. Early myelination involves the dynamic and repetitive
1224 ensheathment of axons which resolves through a low and consistent stabilization rate.
1225 *Elife* **12**, e82111 (2023).
1226 38. Kukley, M., Nishiyama, A. & Dietrich, D. The fate of synaptic input to NG2 glial cells:
1227 Neurons specifically downregulate transmitter release onto differentiating
1228 oligodendroglial cells. *J. Neurosci.* **30**, 8320–8331 (2010).
1229 39. De Biase, L. M., Nishiyama, A. & Bergles, D. E. Excitability and synaptic communication
1230 within the oligodendrocyte lineage. *J. Neurosci.* **30**, 3600–3611 (2010).
1231 40. Hildebrand, D. G. C. *et al.* Whole-brain serial-section electron microscopy in larval

1232 zebrafish. *Nature* **545**, 345–349 (2017).

1233 41. Almeida, A. R. & Macklin, W. B. Early myelination involves the dynamic and repetitive
1234 ensheathment of axons which resolves through a low and consistent stabilization rate.
1235 *Elife* **12**, e82111 (2023).

1236 42. Baraban, M., Koudelka, S. & Lyons, D. A. Ca 2+ activity signatures of myelin sheath
1237 formation and growth in vivo. *Nat. Neurosci.* **21**, 19–25 (2018).

1238 43. Lu, T.-Y., Hanumaihgari, P., Hsu, E. T., Agarwal, A. & Bergles, D. E. Norepinephrine
1239 enhances oligodendrocyte precursor cell calcium dynamics in the cerebral cortex during
1240 arousal. *bioRxiv* 2022.08.25.505119 (2022) doi:10.1101/2022.08.25.505119.

1241 44. Fiore, F. *et al.* Norepinephrine regulates Ca²⁺ signals and fate of
1242 oligodendrocyte progenitor cells in the cortex. *bioRxiv* 2022.08.31.505555 (2022)
1243 doi:10.1101/2022.08.31.505555.

1244 45. Koudelka, S. *et al.* Individual Neuronal Subtypes Exhibit Diversity in CNS Myelination
1245 Mediated by Synaptic Vesicle Release. *Curr. Biol.* **26**, 1447–1455 (2016).

1246 46. Shipman, S. L. *et al.* Functional dependence of neuroligin on a new non-PDZ intracellular
1247 domain. *Nat. Neurosci.* **14**, 718–726 (2011).

1248 47. Almeida, A. R. & Macklin, W. B. Early myelination involves the dynamic and repetitive
1249 ensheathment of axons which resolves through a low and consistent stabilization rate.
1250 *bioRxiv* 2022.07.17.500324 (2022) doi:10.1101/2022.07.17.500324.

1251 48. Osso, L. A., Rankin, K. A. & Chan, J. R. Experience-dependent myelination following stress
1252 is mediated by the neuropeptide dynorphin. *Neuron* **109**, 3619-3632.e5 (2021).

1253 49. Almeida, R. G. *et al.* Myelination induces axonal hotspots of synaptic vesicle fusion that

1254 promote sheath growth. *Curr. Biol.* **31**, 3743-3754.e5 (2021).

1255 50. Gerrow, K. *et al.* A preformed complex of postsynaptic proteins is involved in excitatory
1256 synapse development. *Neuron* **49**, 547–562 (2006).

1257 51. Panzer, J. A. *et al.* Neuromuscular synaptogenesis in wild-type and mutant zebrafish. *Dev.*
1258 *Biol.* **285**, 340–357 (2005).

1259 52. Wierenga, C. J., Becker, N. & Bonhoeffer, T. GABAergic synapses are formed without the
1260 involvement of dendritic protrusions. *Nat. Neurosci.* **11**, 1044–1052 (2008).

1261 53. Villa, K. L. *et al.* Inhibitory Synapses Are Repeatedly Assembled and Removed at
1262 Persistent Sites In Vivo. *Neuron* **89**, 756–769 (2016).

1263 54. Wake, H., Lee, P. R. & Fields, R. D. Control of local protein synthesis and initial events in
1264 myelination by action potentials. *Science (80-.).* **333**, 1647–1651 (2011).

1265 55. Proctor, D. T. *et al.* Axo-glial communication through neurexin-neuroligin signaling
1266 regulates myelination and oligodendrocyte differentiation. *Glia* **63**, 2023–2039 (2015).

1267 56. Stogsdill, J. A. *et al.* Astrocytic neuroligins control astrocyte morphogenesis and
1268 synaptogenesis. *Nature* **551**, 192–197 (2017).

1269 57. Waggener, C. T., Dupree, J. L., Elgersma, Y. & Fuss, B. CaMKIIβ regulates oligodendrocyte
1270 maturation and CNS myelination. *J. Neurosci.* **33**, 10453–10458 (2013).

1271 58. Mitra, S. K., Hanson, D. A. & Schlaepfer, D. D. Focal adhesion kinase: In command and
1272 control of cell motility. *Nature Reviews Molecular Cell Biology* vol. 6 56–68 at
1273 https://doi.org/10.1038/nrm1549 (2005).

1274 59. Venkatesh, H. S. *et al.* Neuronal activity promotes glioma growth through neuroligin-3
1275 secretion. *Cell* **161**, 803–816 (2015).

1276 60. Uchigashima, M., Ohtsuka, T., Kobayashi, K. & Watanabe, M. Dopamine synapse is a
1277 neuroligin-2-mediated contact between dopaminergic presynaptic and GABAergic
1278 postsynaptic structures. *Proc. Natl. Acad. Sci. U. S. A.* **113**, 4206–4211 (2016).
1279 61. Almeida, R. G. & Lyons, D. A. Intersectional gene expression in zebrafish using the split
1280 KalTA4 system. *Zebrafish* **12**, 377–386 (2015).
1281 62. Meyer, M. P., Trimmer, J. S., Gilthorpe, J. D. & Smith, S. J. Characterization of zebrafish
1282 PSD-95 gene family members. *J. Neurobiol.* **63**, 91–105 (2005).
1283 63. Easley-Neal, C., Fierro, J., Buchanan, J. A. & Washbourne, P. Late Recruitment of Synapsin
1284 to Nascent Synapses Is Regulated by Cdk5. *Cell Rep.* **3**, 1199–1212 (2013).
1285 64. Sheets, L., Trapani, J. G., Mo, W., Obholzer, N. & Nicolson, T. Ribeye is required for
1286 presynaptic CaV1.3a channel localization and afferent innervation of sensory hair cells.
1287 *Development* **138**, 1309–1319 (2011).
1288 65. Fuhrmann, J. C. *et al.* Gephyrin interacts with dynein light chains 1 and 2, components of
1289 motor protein complexes. *J. Neurosci.* **22**, 5393–5402 (2002).
1290 66. Smolinsky, B., Eichler, S. A., Buchmeier, S., Meier, J. C. & Schwarz, G. Splice-specific
1291 functions of gephyrin in molybdenum cofactor biosynthesis. *J. Biol. Chem.* **283**, 17370–
1292 17379 (2008).
1293 67. Craven, S. E., El-Husseini, A. E. & Bredt, D. S. Synaptic targeting of the postsynaptic
1294 density protein PSD-95 mediated by lipid and protein motifs. *Neuron* **22**, 497–509 (1999).
1295 68. Topinka, J. R. & Bredt, D. S. N-terminal palmitoylation of PSD-95 regulates association
1296 with cell membranes and interaction with K+ channel K(v)1.4. *Neuron* **20**, 125–134 (1998).
1297 69. Chen, T. W. *et al.* Ultrasensitive fluorescent proteins for imaging neuronal activity.

1298 *Nature* **499**, 295–300 (2013).

1299 70. Kwan, K. M. *et al.* The Tol2kit: A multisite gateway-based construction Kit for Tol2

1300 transposon transgenesis constructs. *Dev. Dyn.* **236**, 3088–3099 (2007).

1301 71. Wyart, C. *et al.* Optogenetic dissection of a behavioural module in the vertebrate spinal

1302 cord. *Nature* **461**, 407–410 (2009).

1303 72. Di Donato, V. *et al.* 2C-Cas9: A versatile tool for clonal analysis of gene function. *Genome*

1304 *Res.* **26**, 681–692 (2016).

1305 73. Tinevez, J. Y. *et al.* TrackMate: An open and extensible platform for single-particle

1306 tracking. *Methods* **115**, 80–90 (2017).

1307 74. Srinivasan, R. *et al.* Ca2+ signaling in astrocytes from Ip3r2 -/- mice in brain slices and

1308 during startle responses in vivo. *Nat. Neurosci.* **18**, 708–717 (2015).

1309

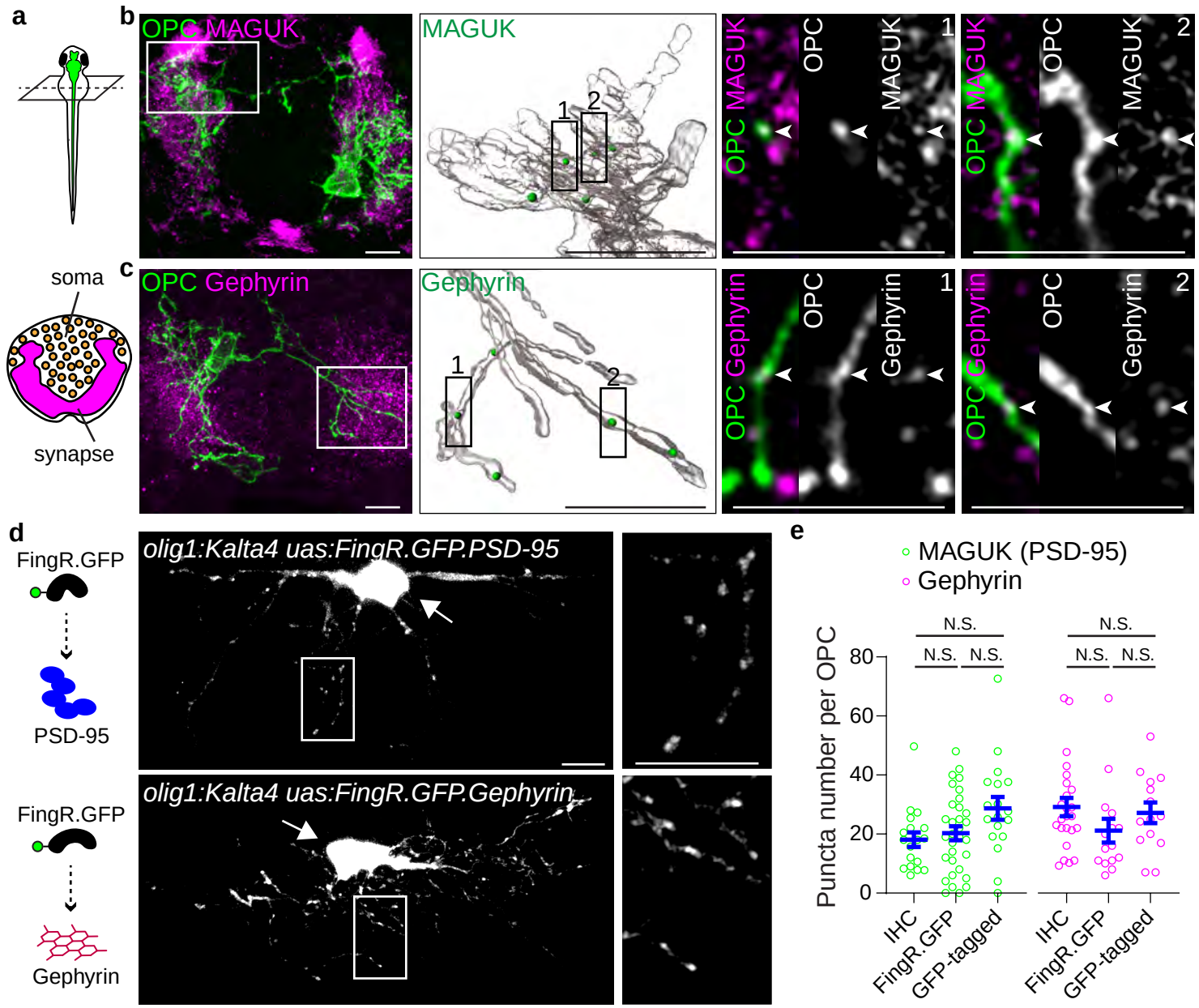
a
b
OPC MAGUK
MAGUK
1
2
OPC MAGUK
OPC
MAGUK
c
soma
synapse
OPC Gephyrin
Gephyrin
OPC Gephyrin
d
FingR.GFP
PSD-95
olig1:Kalta4 uas:FingR.GFP.PSD-95
FingR.GFP
Gephyrin
olig1:Kalta4 uas:FingR.GFP.Gephyrin
e
MAGUK (PSD-95)
Gephyrin
Puncta number per OPC
N.S.
IHC
FingR.GFP
GFP-tagged

Figure 1

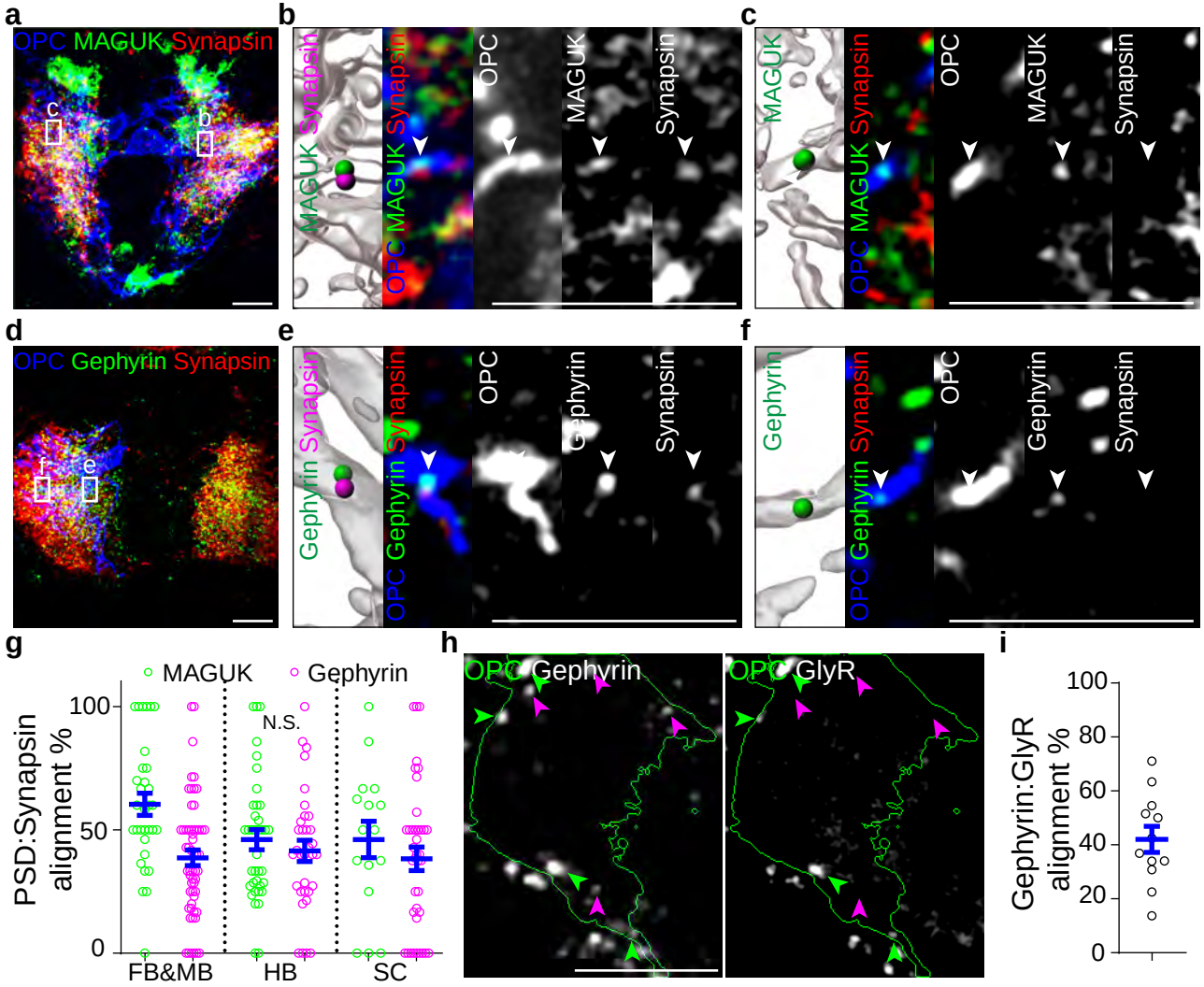
a
OPC MAGUK Synapsin
c
b
b
MAGUK Synapsin
OPC MAGUK Synapsin
OPC
MAGUK
Synapsin
c
MAGUK
OPC MAGUK Synapsin
OPC
MAGUK
Synapsin
d
OPC Gephyrin Synapsin
f
e
e
Gephyrin Synapsin
OPC Gephyrin Synapsin
OPC
Gephyrin
Synapsin
f
Gephyrin
OPC Gephyrin Synapsin
OPC
Gephyrin
Synapsin
g
MAGUK
Gephyrin
PSD:Synapsin alignment %
100
50
0
N.S.
FB&MB
HB
SC
h
OPC Gephyrin
OPC GlyR
i
Gephyrin:GlyR alignment %
100
80
60
40
20
0

Figure 2

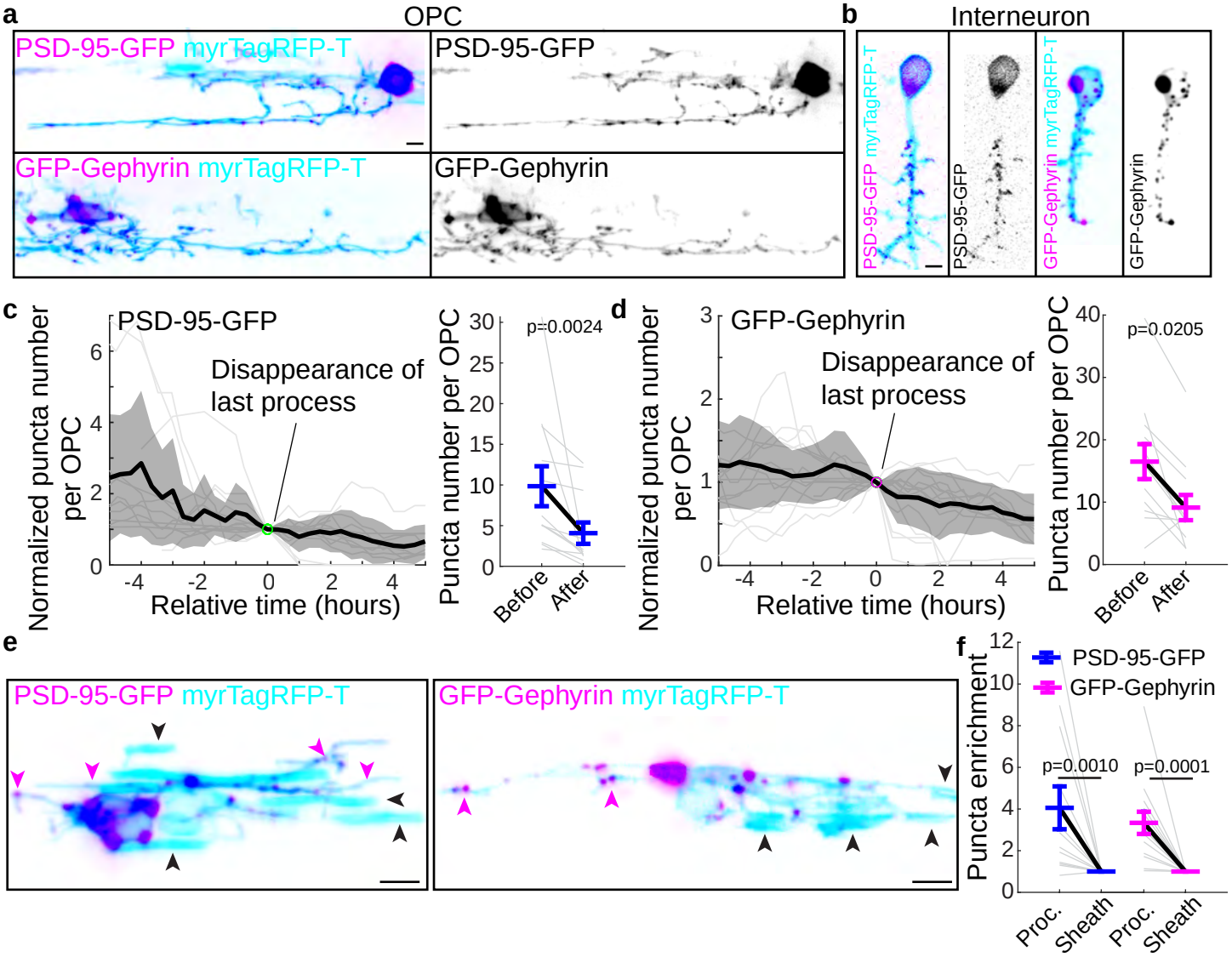
a
OPC
PSD-95-GFP myrTagRFP-T
PSD-95-GFP
GFP-Gephyrin myrTagRFP-T
GFP-Gephyrin
b
Interneuron
PSD-95-GFP myrTagRFP-T
PSD-95-GFP
GFP-Gephyrin myrTagRFP-T
GFP-Gephyrin
c
PSD-95-GFP
Disappearance of last process
Normalized puncta number per OPC
Relative time (hours)
Puncta number per OPC
p=0.0024
Before
After
d
GFP-Gephyrin
Disappearance of last process
Normalized puncta number per OPC
Relative time (hours)
Puncta number per OPC
p=0.0205
Before
After
e
PSD-95-GFP myrTagRFP-T
GFP-Gephyrin myrTagRFP-T
f
PSD-95-GFP
GFP-Gephyrin
Puncta enrichment
p=0.0010
p=0.0001
Proc.
Sheath
Proc.
Sheath

Figure 3

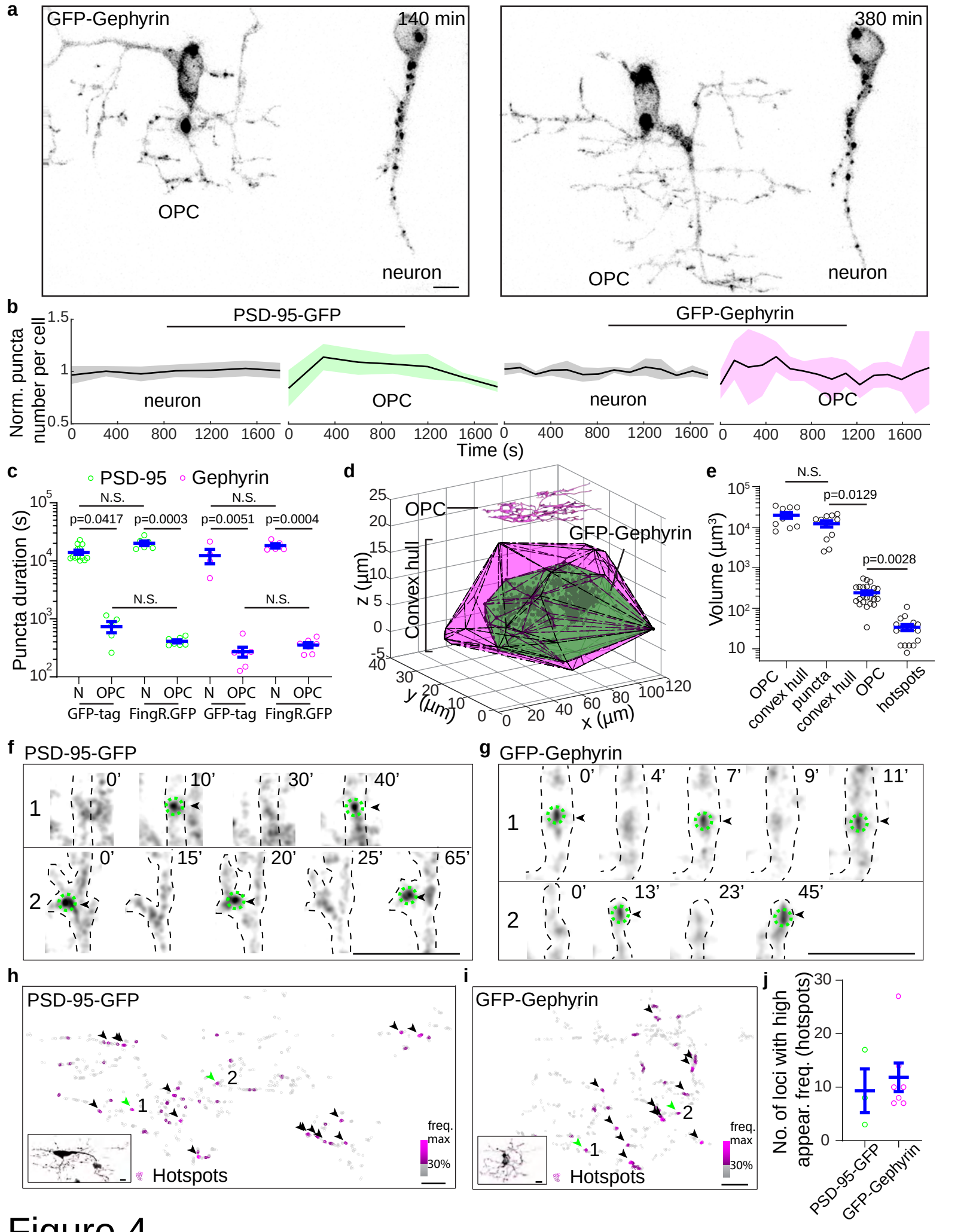
a
GFP-Gephyrin
140 min
OPC
neuron
380 min
OPC
neuron
b
PSD-95-GFP
GFP-Gephyrin
Norm. puncta number per cell
neuron
OPC
neuron
OPC
Time (s)
c
PSD-95
Gephyrin
Puncta duration (s)
N.S.
p=0.0417
p=0.0003
N.S.
p=0.0051
p=0.0004
N.S.
N.S.
N OPC N OPC N OPC N OPC
GFP-tag FingR.GFP GFP-tag FingR.GFP
d
OPC
GFP-Gephyrin
Convex hull
z (µm)
y (µm)
x (µm)
e
N.S.
p=0.0129
p=0.0028
Volume (µm³)
OPC
convex hull
puncta
convex hull
OPC
hotspots
f
PSD-95-GFP
0'
10'
30'
40'
0'
15'
20'
25'
65'
g
GFP-Gephyrin
0'
4'
7'
9'
11'
0'
13'
23'
45'
h
PSD-95-GFP
freq.
max
30%
Hotspots
i
GFP-Gephyrin
freq.
max
30%
Hotspots
j
No. of loci with high appear. freq. (hotspots)
PSD-95-GFP
GFP-Gephyrin

Figure 4

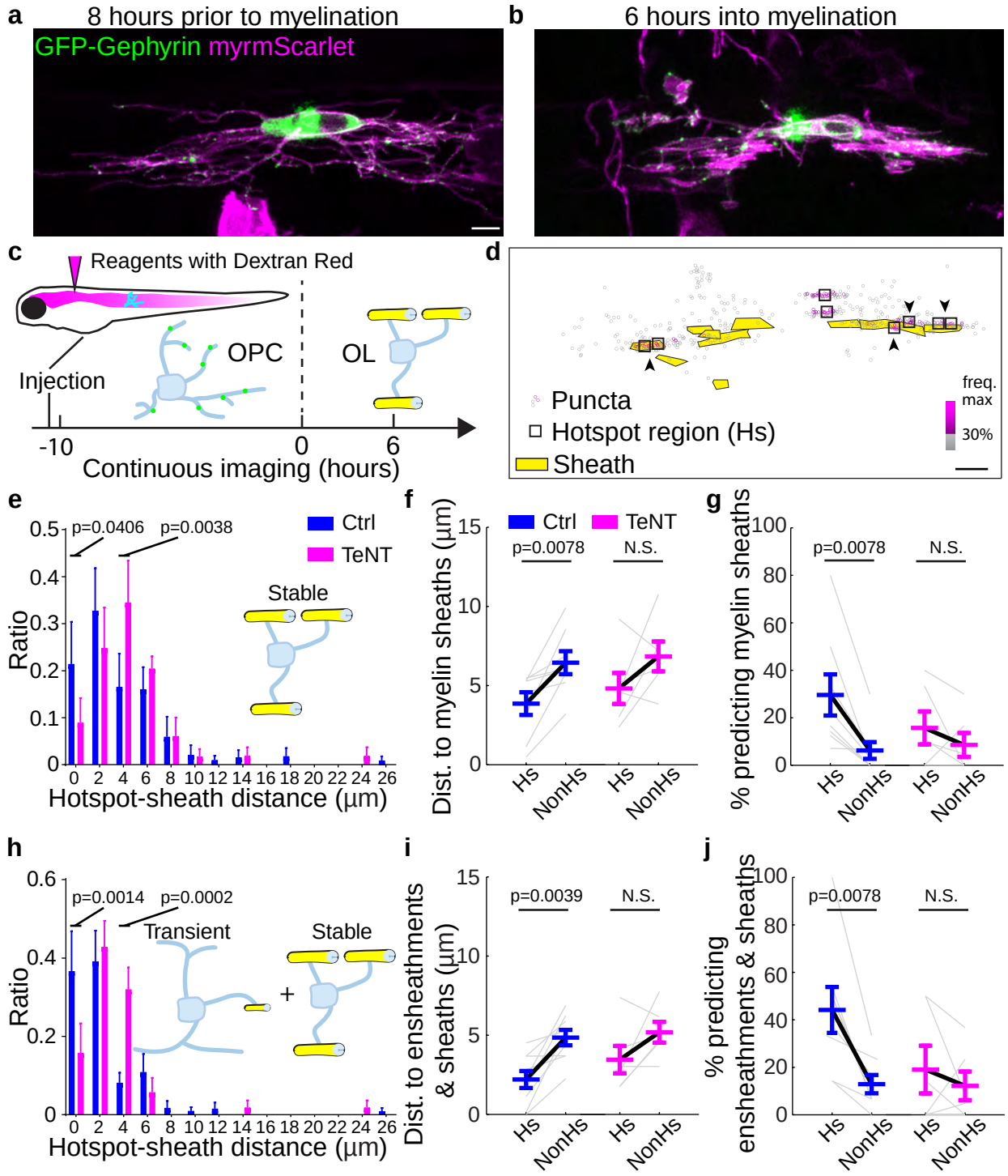
a
8 hours prior to myelination
GFP-Gephyrin myrmScarlet
b
6 hours into myelination
c
Reagents with Dextran Red
Injection
OPC
OL
-10
0
6
Continuous imaging (hours)
d
Puncta
Hotspot region (Hs)
Sheath
freq.
max
30%
e
p=0.0406
p=0.0038
Ctrl
TeNT
Stable
Ratio
Hotspot-sheath distance (µm)
f
Ctrl
TeNT
p=0.0078
N.S.
Dist. to myelin sheaths (µm)
HS
NonHS
g
p=0.0078
N.S.
% predicting myelin sheaths
h
p=0.0014
p=0.0002
Transient
Stable
Ratio
Hotspot-sheath distance (µm)
i
p=0.0039
N.S.
Dist. to ensheathments & sheaths (µm)
j
p=0.0078
N.S.
% predicting ensheathments & sheaths

Figure 5

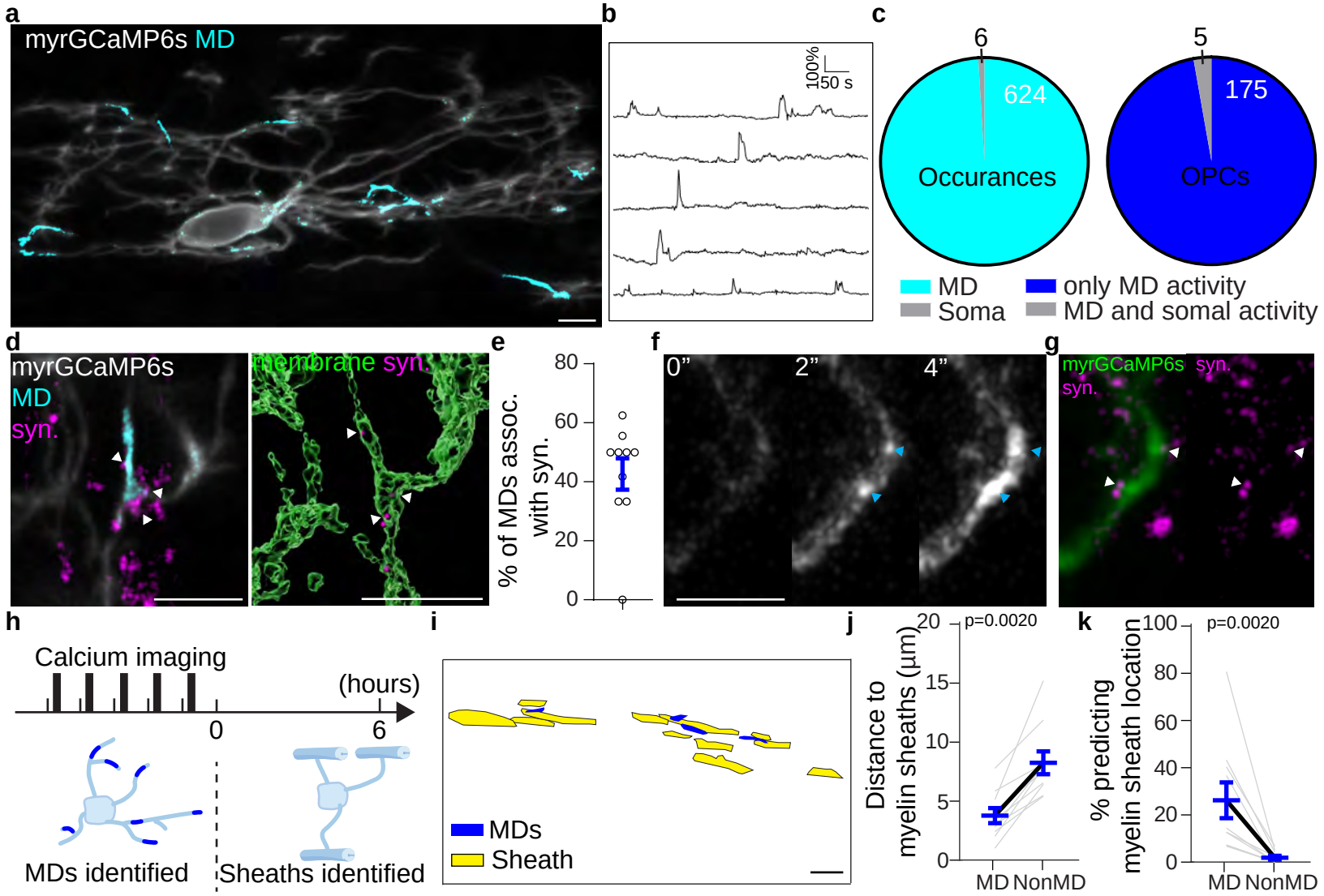
a
myrGCaMP6s MD
b
100%
150 s
c
6
624
Occurances
5
175
OPCs
MD
Soma
only MD activity
MD and somal activity
d
myrGCaMP6s
MD
syn.
membrane syn.
e
% of MDs assoc. with syn.
80
60
40
20
0
f
0"
2"
4"
g
myrGCaMP6s
syn.
syn.
h
Calcium imaging
(hours)
0
6
MDs identified
Sheaths identified
i
MDs
Sheath
j
Distance to myelin sheaths (µm)
20
15
10
5
0
p=0.0020
MD
NonMD
k
% predicting myelin sheath location
100
80
60
40
20
0
p=0.0020
MD
NonMD

Figure 6

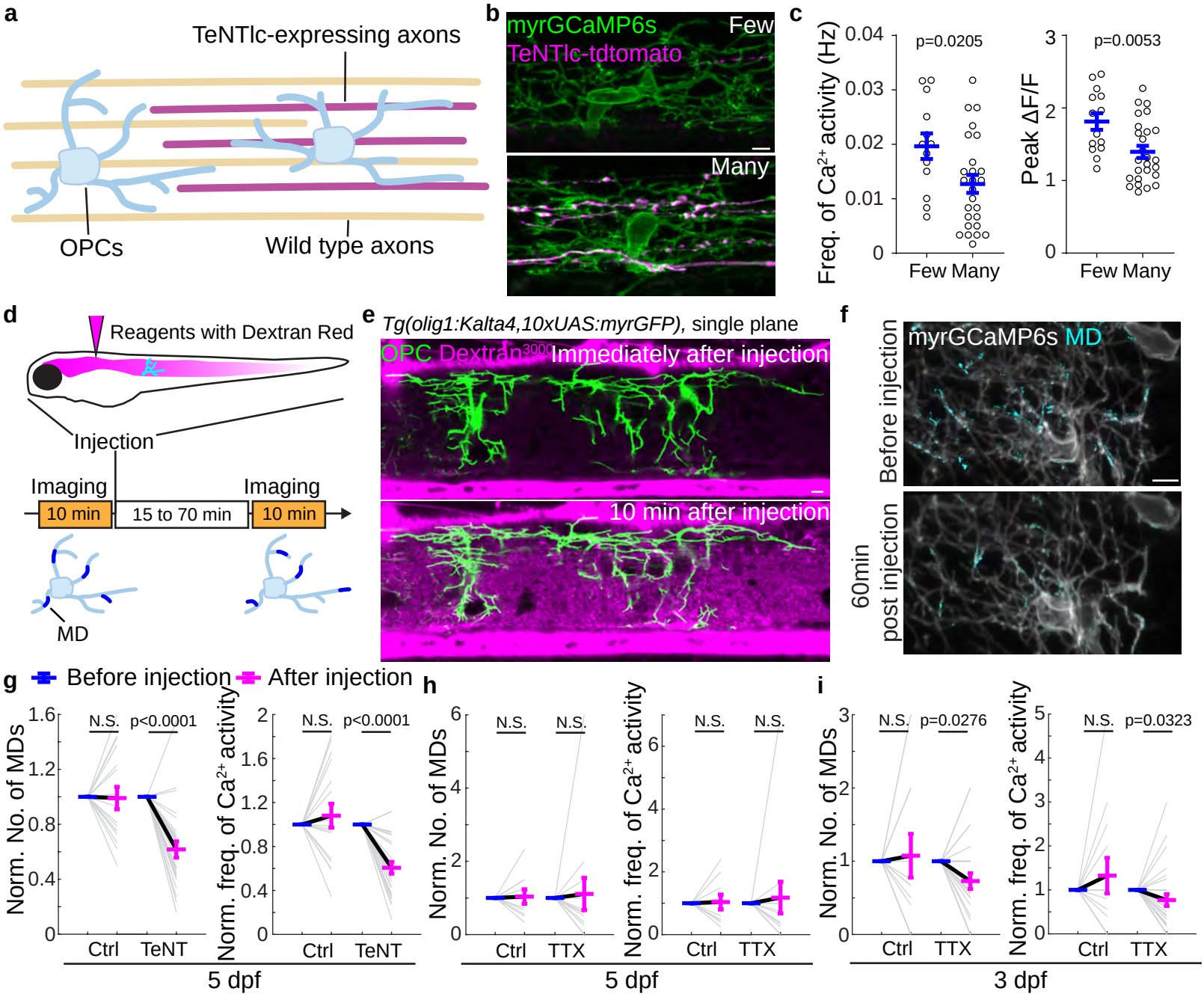
a
TeNTlc-expressing axons
OPCs
Wild type axons
b
myrGCaMP6s
TeNTlc-tdtomato
Few
Many
c
Freq. of Ca2+ activity (Hz)
p=0.0205
Peak ΔF/F
p=0.0053
Few Many
Few Many
d
Reagents with Dextran Red
Injection
Imaging
10 min
15 to 70 min
Imaging
10 min
MD
e
Tg(olig1:Kalta4,10xUAS:myrGFP), single plane
OPC Dextran3000
Immediately after injection
10 min after injection
f
Before injection
myrGCaMP6s MD
60min post injection
g
Before injection
After injection
Norm. No. of MDs
N.S.
p<0.0001
Norm. freq. of Ca2+ activity
N.S.
p<0.0001
Ctrl
TeNT
Ctrl
TeNT
5 dpf
h
Norm. No. of MDs
N.S.
N.S.
Norm. freq. of Ca2+ activity
N.S.
N.S.
Ctrl
TTX
Ctrl
TTX
5 dpf
i
Norm. No. of MDs
N.S.
p=0.0276
Norm. freq. of Ca2+ activity
N.S.
p=0.0323
Ctrl
TTX
Ctrl
TTX
3 dpf

Figure 7

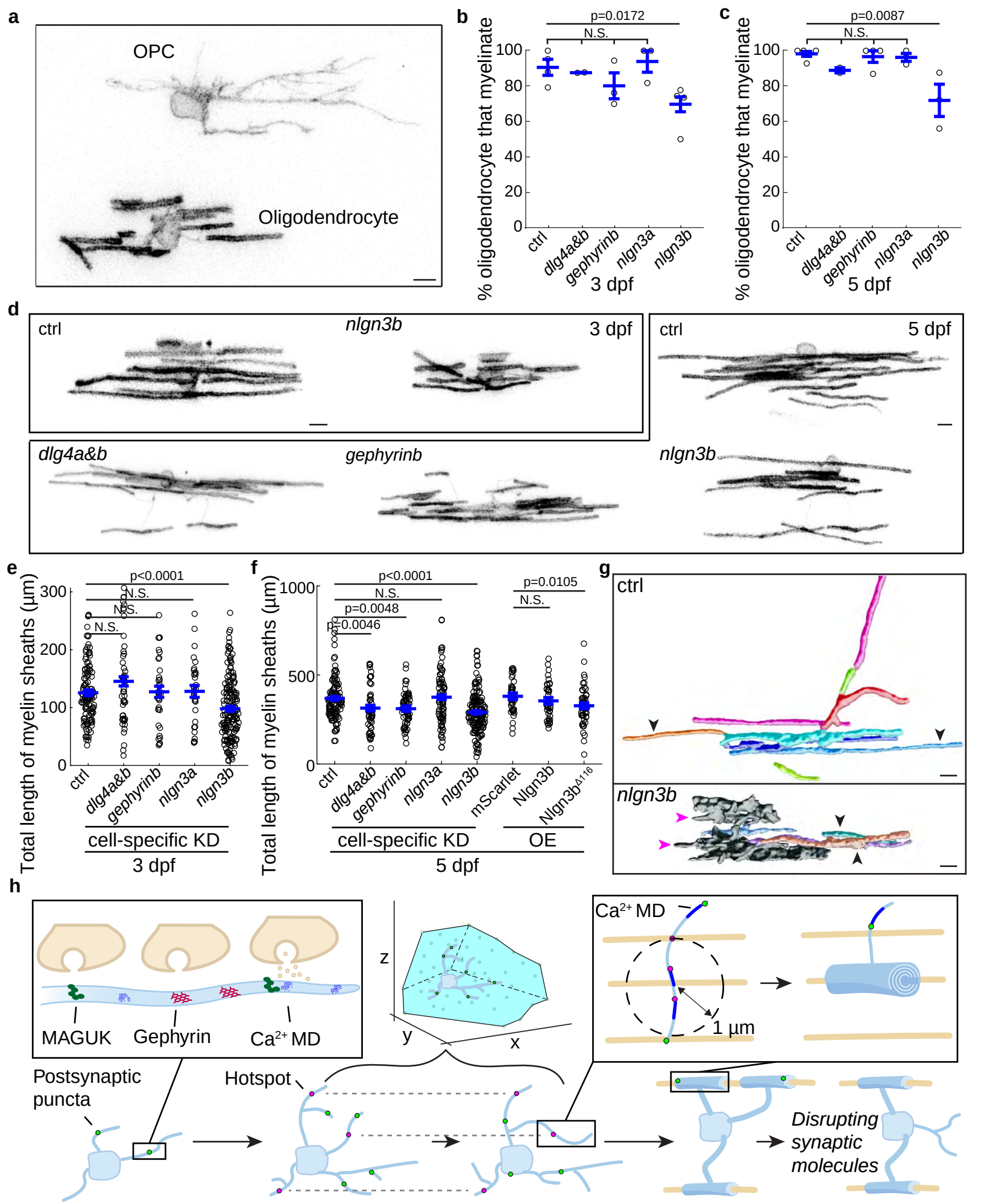
a
OPC
Oligodendrocyte
b
p=0.0172
N.S.
% oligodendrocyte that myelinate
ctrl
dlg4a&b
gephyrinb
nlgn3a
nlgn3b
3 dpf
c
p=0.0087
N.S.
5 dpf
d
ctrl
nlgn3b
3 dpf
5 dpf
dlg4a&b
gephyrinb
e
p<0.0001
N.S.
Total length of myelin sheaths (µm)
cell-specific KD
3 dpf
f
p<0.0001
N.S.
p=0.0048
p=0.0046
p=0.0105
mScarlet
Nlgn3b
Nlgn3b^Δ116
OE
5 dpf
g
h
MAGUK
Gephyrin
Ca2+ MD
z
y
x
1 µm
Postsynaptic puncta
Hotspot
Disrupting synaptic molecules

Figure 8